

September 20, 2018

# Chandra Multiwavelength Project

## X-ray Point Source Number Counts and the Cosmic X-ray Background

Minsun Kim<sup>1,2</sup>, Belinda J. Wilkes<sup>1</sup>, Dong-Woo Kim<sup>1</sup>, Paul J. Green<sup>1</sup>, Wayne A. Barkhouse<sup>3</sup>,  
Myung Gyoon Lee<sup>2</sup>, John D. Silverman<sup>4</sup>, and Harvey D. Tananbaum<sup>1</sup>

mkim@cfa.harvard.edu

### ABSTRACT

We present the *Chandra* Multiwavelength Project (ChaMP) X-ray point source number counts and the cosmic X-ray background (CXRB) flux densities in multiple energy bands. From the ChaMP X-ray point source catalog,  $\sim 5,500$  sources are selected covering  $9.6 \text{ deg}^2$  in sky area. To quantitatively characterize the sensitivity and completeness of the ChaMP sample, we perform extensive simulations. We also include the ChaMP+CDFs (*Chandra* Deep Fields) number counts to cover large flux ranges from  $2 \times 10^{-17}$  to  $2.4 \times 10^{-12}$  (0.5-2 keV) and from  $2 \times 10^{-16}$  to  $7.1 \times 10^{-12}$  (2-8 keV)  $\text{erg cm}^{-2} \text{ sec}^{-1}$ . The ChaMP and the ChaMP+CDFs differential number counts are well fitted with a broken power law. The best fit faint and bright power indices are  $1.49^{+0.02}_{-0.02}$  and  $2.36^{+0.05}_{-0.05}$  (0.5-2 keV), and  $1.58^{+0.01}_{-0.01}$  and  $2.59^{+0.06}_{-0.05}$  (2-8 keV), respectively. We detect breaks in the differential number counts and they appear at different fluxes in different energy bands. Assuming a single power law model for a source spectrum, we find that the same population(s) of soft X-ray sources causes the break in the differential number counts for all energy bands. We measure the resolved CXRB flux densities from the ChaMP and the ChaMP+CDFs number counts with and without bright target sources. Adding the known unresolved CXRB to the ChaMP+CDF resolved CXRB, we also estimate total CXRB flux densities. The fractions of the resolved CXRB without target sources are  $78^{+1}_{-1}\%$  and  $81^{+2}_{-2}\%$  in the 0.5-2 keV and 2-8 keV bands, respectively, somewhat lower, though generally consistent with earlier numbers since their large errors. These fractions increase by  $\sim 1\%$  when target sources are included.

---

<sup>1</sup>Harvard-Smithsonian Center for Astrophysics, 60 Garden Street, Cambridge, MA 02138, USA

<sup>2</sup>Department of Physics and Astronomy, Astronomy Program, Seoul National University, Seoul 151-742, Korea

<sup>3</sup>Department of Astronomy, University of Illinois at Urbana-Champaign, Urbana, IL 61801, USA

<sup>4</sup>Max-Planck-Institut für extraterrestrische Physik, D-84571 Garching, Germany

*Subject headings:* cosmology: observations — methods: data analysis — X-rays: X-ray number counts — X-rays: cosmic X-ray background — surveys: Chandra Multiwavelength Project

## 1. Introduction

What is the origin and nature of the cosmic X-ray background (hereafter CXRB)? Can detected X-ray sources account for the CXRB? The CXRB consists of resolved and unresolved components. The resolved CXRB originates in discrete sources such as point and extended sources while diffuse components and faint sources which are below current flux limits contribute to the unresolved CXRB. The contribution of discrete X-ray sources to the CXRB can be directly measured from their number counts. Using the deep surveys of *ROSAT*, *Chandra*, and *XMM-Newton*, the X-ray number counts have been determined down to flux limits of  $\sim 2.3 \times 10^{-17}$  (0.5-2 keV),  $\sim 2.0 \times 10^{-16}$  (2-8 keV), and  $\sim 1.2 \times 10^{-15}$  (5-10 keV)  $\text{erg cm}^{-2} \text{sec}^{-1}$  and  $\approx 80 - 90\%$  of the CXRB is resolved into discrete X-ray sources in the 0.5-2 keV and 2-8 keV (see Brandt and Hasinger (2005) for a detailed review). In this study, using the *Chandra* Multiwavelength Project (ChaMP) and the *Chandra* Deep Fields (CDFs) data, which include the largest number of sources and cover the widest sky area and flux range from a single satellite *Chandra* to date, we provide statistically robust X-ray number counts and CXRB flux densities without cross-calibration problem which is usually included in data from multiple satellites. Also we study the X-ray number counts in multiple energy bands to systematically understand their behavior in each energy band.

There have been many similar studies. Using the *Chandra* survey of SSA13, Mushotzky et al. (2000) presented the X-ray number counts in the 0.5-2 keV and 2-10 keV bands, and suggested that detected hard X-ray sources account for at least 75% of the hard CXRB and that the mean X-ray spectrum of these sources is in good agreement with that of the background. Cowie et al. (2002) presented the 2-8 keV number counts from the CDF-S and CDF-N with SSA13/SSA22 and Rosati et al. (2002) presented those of the CDF-S, finding that at most  $\sim 10\%$  ( $\sim 15\%$ ) of the CXRB is unresolved in the soft (hard) energy band. Manners et al. (2003) presented the X-ray number counts in the 0.5-2, 2-8, and 0.5-8 keV using the ELAIS survey data. Moretti et al. (2003) (hereafter M03) presented the X-ray number counts in the 0.5-2 and 2-10 keV from combining data from three different surveys (*ROSAT*, *Chandra*, and *XMM-Newton*). They concluded that 95% and 89% of the soft and hard CXRB respectively can be resolved into discrete X-ray sources. Bauer et al. (2004) (hereafter B04) combined the CDF-N and CDF-S data and measured the contributions of the faint X-ray source populations to the CXRB. They found that 90% (0.5-2 keV) and 93% (2-8 keV) of the total CXRB was resolved into discrete sources. Basilakos et al. (2005) pre-

sented the number counts of the *XMM-Newton*/2dF survey in the 0.5-2 and 0.5-8 keV bands and Chiappetti et al. (2005) presented the number counts of the *XMM*-LSS survey in the 0.5-2 and 2-10 keV bands. Worsley et al. (2005) found that the resolved fractions of the CXRB are  $\sim 85\%$  (0.5-2 keV),  $\sim 80\%$  (2-10 keV), and  $\sim 50\%$  at  $\gtrsim 8$  keV, respectively. Recently, Hickox & Markevitch (2006) (hereafter HM06) directly measured the absolute unresolved CXRB from *Chandra* Deep Fields images after excluding point and extended sources in those fields. They also estimated the resolved X-ray source intensity from the CDFs and from the number counts for brighter sources (Vikhlinin et al. 1995; Moretti et al. 2003), and then estimated the total CXRB flux density by combining the two. They found that the resolved fractions of the CXRB are  $77 \pm 3\%$  (1-2 keV) and  $80 \pm 8\%$  (2-8 keV), respectively. Until now, using the *ROSAT*, *XMM*, and *Chandra* data, these many studies have revealed that  $\sim 80\%$  of the CXRB is resolved into discrete X-ray sources in the 0.5-2 keV and 2-8 keV bands; however, the resolved fraction of the CXRB significantly decreases at  $\gtrsim 8$  keV.

The ChaMP is a serendipitous, wide area survey covering intermediate and high fluxes using *Chandra* archival data. Kim, D.-W. et al. (2004a) presented the initial ChaMP catalog which contains  $\sim 800$  X-ray point sources in the central region of 62 of 149 ChaMP fields. From the initial ChaMP catalog, Kim, D.-W. et al. (2004b) (hereafter KD04) presented X-ray number counts in the 0.5-2 keV and 2-8 keV bands. To avoid the incompleteness of the selected fields, they selected sources having large X-ray source counts ( $> 20$ ) and located close to on-axis ( $< 400''$ ). The selected sample covered  $\sim 1.1 \text{ deg}^2$  in sky area. In flux range from  $10^{-15}$  to  $10^{-13}$  (0.5-2 keV), they detected the break in the differential number counts. However, due to the shallow flux limit, they could not detect the break in the 2-8 keV band.

In this study, we use the latest ChaMP X-ray point source catalog which contains  $\sim 6,800$  X-ray point sources in 149 ChaMP fields with sky coverage area of  $\sim 10 \text{ deg}^2$  (Kim, M. et al. 2006, hereafter KM06) to determine the X-ray point source number counts in 6 energy bands. To correct for incompleteness, Eddington bias, and instrumental effects, and to include large off axis angles (up to  $\sim 15'$ ) and faint (down to  $\sim 5$  source counts) sources, we perform extensive simulations to calculate the sky coverage of the selected sources as a function of flux. Using this large sample and the simulation results, we present the X-ray point source number counts which fully cover the break flux in each energy band with small statistical errors. Due to the wide flux range of the sample, we detect breaks in the differential number counts in all energy bands and investigate what causes the different break flux in different energy band. We also investigate the nature and the origin of the break in the differential number counts using hardness ratio  $HR = (H_c - S_c)/(H_c + S_c)$ , see Table 1 for energy band definition) and redshift distribution of the X-ray sources. We also combine the ChaMP and CDFs (hereafter ChaMP+CDFs) number counts to cover the full available flux range. From the ChaMP and the ChaMP+CDFs number counts, we estimate the resolved CXRB flux densities in 6 energy bands. By adding the known unresolved CXRB (HM06) to the resolved

ChaMP+CDFs CXRB flux density, we estimate the total CXRB flux densities in the 0.5-2 keV, 1-2 keV, and 2-8 keV bands.

In §2, we briefly describe the ChaMP data selection. In §3, we describe the method and results of the ChaMP simulations. In §4, the ChaMP and the ChaMP+CDFs number counts are presented in 6 energy bands and are compared with previous studies. In §5, we study the nature and origin of the break flux in the number counts. In §6, we estimate the resolved CXRB flux densities in 6 energy bands and the total CXRB flux densities in 3 energy bands. In §7, the summary and conclusions of this study are shown. Throughout this study, quoted errors are for a  $\pm 1\sigma$  confidence level, unless otherwise noted. Although we perform this study in 6 energy bands (see Table 1), we only present the figures in the 0.5-8 keV, 0.5-2 keV, and 2-8 keV bands for simplicity; however, tables include the results in all energy bands. To compare with previous studies, we assume photon indices of  $\Gamma_{ph} = 1.4$  and  $\Gamma_{ph} = 1.7$ ; however, figures only with  $\Gamma_{ph} = 1.4$  are provided.

## 2. The ChaMP Sample Selection

The X-ray point source sample is from the ChaMP X-ray point source catalog (KM06) which consists of  $\sim 6,800$  X-ray sources in 149 *Chandra* archival observations. The ChaMP fields were selected to include ACIS observations at high Galactic latitude,  $|b| > 20^\circ$ . Fields containing large extended sources, planetary objects, PI surveys, and local group galaxies were excluded (Kim, D.-W. et al. 2004a). The ChaMP X-ray point source properties were obtained using a ChaMP-specific pipeline, XPIPE, which uses *wavdetect*<sup>1</sup> detections as source positions and extracts source properties within a given aperture appropriate for the local PSF size (a 95% encircled energy radius at 1.5 keV) using *xapphot* (Kim, E. et al. 2006).

The ChaMP X-ray point source catalog is divided into main and supplementary catalogs. 35 ChaMP fields overlap one another and the supplementary catalog contains sources from the 19 shorter exposure fields among these. To avoid confusion due to duplicated fields, our analysis uses the main ChaMP catalog which contains 130 ChaMP fields. From the main ChaMP catalog, we selected sources in the I0, I1, I2 and I3 CCD chips for 32 ACIS-I observations, and sources in I2, I3, S2, and S3 CCD chips for 98 ACIS-S observations. These sources are located within an off axis angle of  $\sim 15'$ . In addition, we selected sources with signal to noise ratio,  $S/N > 1.5$  corresponding to source counts of  $C \gtrsim 5$ . XPIPE detects sources in the B band (0.3-8 keV, see Table 1 for energy band definitions) and for all energy bands, photometry is performed at the source positions determined in the B band (see §3 in KM06). Therefore, in our sample, it is possible to

---

<sup>1</sup>See <http://cxc.harvard.edu/ciao>.

miss very soft (hard) sources which might be detected only in the soft (hard) band but not detected in the B band. For sources with  $S/N > 1.5$  in the S (H) band, the missing percentage of very soft (hard) sources is 5% (10%), when we assume matching of all possible counterparts in the B and S (H) bands; however, since we perform simulations to correct the incompleteness and bias in the ChaMP fields using the same detection technique as the ChaMP X-ray point source catalog (see §3), these very soft (hard) sources do not introduce an additional error in our number counts.

Since the ChaMP is a *Chandra* archival survey, most ChaMP fields contain target sources selected by the PI and those targets are likely to be biased towards special X-ray populations such as bright AGNs. Therefore, we excluded target sources to derive less-biased X-ray number counts. Our selection results in  $\sim 5,500$  sources in the 0.3-8 keV band from the ChaMP X-ray point source catalog. Table 2 lists the number of sources and the statistical properties of the X-ray sources in each energy band. Figure 1 shows the counts and flux distributions of the final X-ray sample. The median value of the distribution is also plotted.

### 3. The ChaMP Simulations

To determine accurate number counts, it is necessary to correct for the incompleteness of the sample as well as for instrumental effects such as vignetting and the off-axis degradation of the PSF. There are two major techniques to correct these biases, a semi-analytical approach, and a Monte Carlo simulation. The semi-analytical approach is based on the flux limit map of a given field which contains the faintest flux corresponding to the assumed significance level of source detection (Johnson et al. 2003; Cappelluti et al. 2005; Chiappetti et al. 2005). This technique is efficient and reliable; however, it is possible to undercorrect the incompleteness of the field because in this method the source detection probability is a function of only the source counts. The actual source detection probability in a *Chandra* field is a complex function of off axis angle and source counts: the detection probability decreases as off axis angle increases and as source counts decrease (KM06). Therefore, to accurately determine the sky coverage of the ChaMP sample, we performed extensive Monte Carlo simulations to correct incompleteness and biases of sample fields.

#### 3.1. Method

The simulation method is described in detail in KM06 and consists of three parts, (1) generating artificial X-ray sources with MARX<sup>2</sup>, (2) adding them to the observed image, and (3) detecting

---

<sup>2</sup>See <http://space.mit.edu/CXC/MARX/> and MARX 4.0 Technical Manual.

these artificial sources with *wavdetect* and extracting source properties with the *xapphot*. In step (2), we used the real *Chandra* observations to accurately reflect the effects of background counts and source confusion in the ChaMP fields.

We performed simulations using all selected observations and 4 CCD chips in each observation (see §2). We generated 1,000 artificial X-ray sources per sample field which corresponds to  $\sim 13,000$  artificial X-ray sources per  $deg^2$ . The number of sources in each field depends on the effective exposure time of the observation and the neutral hydrogen column density,  $N_H$ , toward the observed region of the sky. On average, 11.7% of the 127,178 artificial X-ray sources are detected in our simulations, a total of 14,932 artificial X-ray sources in 130 ChaMP fields. The number of detected artificial sources is 2.5 times the  $\sim 6,000$  observed sources and this number is statistically sufficient to estimate the properties of the ChaMP sample.

The form of the assumed number counts distribution is not critical because we use the ratio of input to output number of sources to determine the sensitivity (Vikhlinin et al. 1995; Kim, D.-W. and Fabbiano 2003). The actual X-ray differential number counts are described by a broken/double power law with a faint slope of  $\sim -1.5$  and a bright slope of  $\sim -2.5$  (Yang et al. 2004; Basilakos et al. 2005; Chiappetti et al. 2005) in most energy bands; however, the break flux has not been well determined. Therefore, we assumed a cumulative number counts distribution with a single power law with a slope of  $-1$  corresponding to a slope of  $-2$  in the differential number counts, taking the average of the faint and bright slopes from the literature, in the 0.3-8 keV band. From the assumed number count distribution, we selected the artificial source flux randomly. The artificial source fluxes span from  $5 \times 10^{-16}$  to  $5 \times 10^{-10} \text{ erg cm}^{-2} \text{ sec}^{-1}$  in the B band, covering the flux range of the observed ChaMP X-ray point sources ( $6 \times 10^{-16} \sim 6 \times 10^{-12} \text{ erg cm}^{-2} \text{ sec}^{-1}$ ).

The spectrum of the artificial sources was assumed to be a power law ( $F_\nu \propto \nu^{-\Gamma_{ph}}$ ) with a photon index of  $\Gamma_{ph} = 1.7$ , because the photon index of  $\Gamma_{ph}$  for the observed ChaMP sources spans  $\Gamma_{ph} = 1.5 \sim 2$  (KD04, KM06). Tozzi et al. (2006) performed X-ray spectral analysis for 82 X-ray bright sources in the CDF-S, and found a weighted mean value for the slope of the power law spectrum is  $\langle \Gamma_{ph} \rangle \simeq 1.75 \pm 0.02$ . The flux range of these bright sources in the CDF-S overlaps with the faint flux end of the ChaMP sources, therefore, we assumed that the faint ChaMP sources also have a photon index of  $\Gamma_{ph} \sim 1.7$ . We assumed a Galactic absorption,  $N_H$ , (Stark et al. 1992) for each observation; however, we did not include intrinsic absorption for the artificial source spectrum. The spectrum of each X-ray point source was generated using the XSPEC<sup>3</sup> package.

The artificial source's position was randomly selected in each CCD chip area, but was rejected if the source area at a given random position had an exposure map value of less than 10% of the maximum. This requirement is identical to that in the ChaMP X-ray point source catalog reduction

---

<sup>3</sup>See <http://xspec.gsfc.nasa.gov/>.

procedure. To avoid the over-crowding of the artificial sources,  $\sim 250$  artificial sources per CCD were divided into several groups to be added into the observed image: while we did not allow the artificial X-ray point sources to overlap one another, we allowed overlap between artificial and real X-ray sources to provide an estimate of source confusion in each observed field. This resulted in  $\sim 10$  ( $\sim 20$ ) simulated images per ACIS-I (ACIS-S) CCD, corresponding  $\sim 9,100$  CCD images (event files) to run *wavdetect* (*xapphot*). Since  $\sim 11.7\%$  of the artificial sources ( $\sim 14,900$ ) are detected, on average we added only  $\sim 1.6$  artificial sources to each simulated image. The net counts of the overlapping artificial sources with real sources were corrected following the overlapping source correction methods described in §3.2.2 of KM06.

### 3.2. Sky Coverage Area

Using the results of the simulations described in §3.1, Figure 2 shows the number counts for artificial sources in the B band. The number count for sources, whose fluxes were randomly selected from the assumed number counts (*magenta solid line*), agree well with a slope of  $-1$ . However, there are slight statistical fluctuations at fluxes brighter than  $10^{-13} \text{ erg cm}^{-2} \text{ sec}^{-1}$ . due to small number statistics. The random sources were selected per observation (see §3.1) and 1  $\sim$  2 bright sources out of 1,000 sources result in statistical fluctuations in each observation. Also, since we fixed the flux maximum rather than using infinitely bright flux (see §3.1) for random sources, the cumulative number of artificial sources drops at  $\sim 10^{-12} \text{ erg cm}^{-2} \text{ sec}^{-1}$  rather than following a line of slope  $-1$ . Since the aim of our simulations is to correct bias at faint fluxes, we do not require good statistics at bright fluxes. The number counts for artificial sources generated by MARX (*blue dotted line*) and that for artificial sources detected by XPIPE (*red dashed line*) are also displayed. The Eddington bias, that sources with counts near the detection threshold will be preferentially detected when they have upward fluctuations (e.g., Kenter and Murray (2003)), is evident at faint fluxes ( $S < 10^{-14} \text{ erg cm}^{-2} \text{ sec}^{-1}$ ) in the simulated number counts. Near  $\sim 10^{-14} \text{ erg cm}^{-2} \text{ sec}^{-1}$ , the number of detected artificial sources starts to decrease.

Figure 3 displays sky coverage for sources with  $S/N > 1.5$  as a function of flux in 6 energy bands assuming a photon index of  $\Gamma_{ph} = 1.4$ . The sky coverage area is the ratio of the number of detected over input sources at a given flux, multiplied by the total sky area. The full sky area is  $9.6 \text{ deg}^2$ . The geometrical area of a *Chandra* CCD chip is  $0.0196 \text{ deg}^2$ ; however, the net effective area is slightly larger due to the dither. To accurately calculate the effective area, we follow the same method as *xapphot*: all pixels in the exposure map were summed, excluding those pixels with an exposure map value less than 10% of the maximum within the corresponding source area. This criterion automatically excludes pixel positions located near the edge of the CCD chip.

## 4. X-ray Point Source Number Counts

### 4.1. The ChaMP Number Counts

The cumulative number counts for sources brighter than a given flux  $S$ , corrected by the corresponding sky coverage at  $S$ , is:

$$N(> S) = \sum_{S_i > S} \frac{1}{\Omega_i}, \quad (1)$$

where  $S_i$  is the flux of the  $i$ th X-ray point source and  $\Omega_i$  is the sky coverage that is the maximum solid angle covered by the flux  $S_i$ . Using the sources selected in §2 and the corresponding sky coverage derived in §3.2, we derived the cumulative number counts for the ChaMP point sources. Since the differential number count is a derivative form of the cumulative number counts, we derived the differential number counts from the cumulative number counts resulting from equation (1) as follows:

$$\left. \frac{dN}{dS} \right|_i = - \frac{N_{i+1} - N_i}{S_{i+1} - S_i} \quad (2)$$

where  $N_i$  is the cumulative source number at flux  $S_i$ . Since the sky coverage rapidly decreases near the faint flux limit, there are large statistical errors for the number counts in the faint flux regime. Thus, for better statistics, we present the number counts brighter than the flux corresponding to 10% of the full sky coverage. For example, in the 0.5-8 keV band, this flux cut corresponds to  $2 \times 10^{-15} \text{ erg cm}^{-2} \text{ sec}^{-1}$  and 500 sources fainter than this flux are not included in the final number counts. In Figure 4, we display the ChaMP differential number counts (*left panels*) and cumulative number counts (*right panels*) in 3 energy bands. Statistical errors on the number counts are assigned following Gehrels et al. (1986).

The shape of the cumulative number counts is curved rather than a single power law feature and the differential number counts can be fit by a broken power law (Baldi et al. 2002; Kim, D.-W. et al. 2004b) or by a double power law (Cowie et al. 2002; Harrison et al. 2003; Yang et al. 2004; Chiappetti et al. 2005). Since errors for the cumulative number counts are not independent (Murdoch et al. 1973), it is difficult to estimate confidence levels of fitting parameters for the cumulative number counts. Therefore, we fit the differential number count with a broken power law as follows:

$$\frac{dN}{dS} = \begin{cases} K(S/S_{ref})^{-\gamma_1}, & S < S_b, \\ K(S_b/S_{ref})^{(\gamma_2-\gamma_1)}(S/S_{ref})^{-\gamma_2}, & S \geq S_b, \end{cases} \quad (3)$$

where  $K$  is a normalization constant and  $S_{ref}$  is a normalization flux. In this study, we set a normalization flux of  $S_{ref} = 10^{-15} \text{ erg cm}^{-2} \text{ sec}^{-1}$ .  $S_b$  is the break flux at which the slope of the differential number count changes.  $\gamma_1$  and  $\gamma_2$  are faint and bright power indices. The best fit



parameters for the differential number counts are listed in Table 3 for photon indices of  $\Gamma_{ph} = 1.4$  and  $\Gamma_{ph} = 1.7$ . The photon index  $\Gamma_{ph}$  hardly affects  $\gamma_1$  and  $\gamma_2$ , but it shifts  $S_b$  somewhat. We display the best fit results in the left panels of Figure 4. In all energy bands, we detected breaks and they appear at different fluxes in different energy bands. We discuss the break flux of the differential number count in more detail in §5.

By integrating equation (3), we can derive a formula for the cumulative number count as follows:

$$N(> S) = \int \frac{dN}{dS} dS', \quad (4)$$

therefore,

$$N(> S) = \begin{cases} K \left( \frac{1}{1-\gamma_1} - \frac{1}{1-\gamma_2} \right) (S_b/S_{ref})^{(1-\gamma_1)} + K \left( \frac{1}{\gamma_1-1} \right) (S/S_{ref})^{(1-\gamma_1)}, & S < S_b, \\ K \left( \frac{1}{\gamma_2-1} \right) (S_b/S_{ref})^{(\gamma_2-\gamma_1)} (S/S_{ref})^{(1-\gamma_2)}, & S \geq S_b. \end{cases} \quad (5)$$

where definitions of parameters are the same as equation (3). Using the best fit parameters derived from the differential number counts, we also plot the best fit results for the cumulative number counts in the right panels of Figure 4.

## 4.2. The ChaMP+CDFs Number Counts

To measure the discrete X-ray source contributions to the CXRB, it is important to derive the number counts over a wide range of flux. So far, M03 have presented the widest flux range of number counts using a combination of three different surveys with *ROSAT*, *Chandra*, and *XMM-Newton*. Due to the different calibrations of each satellite, it is possible that additional systematic errors are introduced for this combined survey data. The ChaMP is a medium depth survey which covers the break flux regime in each energy band but with a faint flux limit too shallow to estimate the resolved CXRB. Therefore, to cover the faint flux regime as well, we decided to use the CDFs as well as the ChaMP data to determine the number counts. Since the ChaMP and the CDFs are from the same satellite, *Chandra*, they provide number counts over a wide flux range without systematic errors due to different calibrations.

The cumulative CDFs number counts (B04) are provided by *Chandra Deep Field* web site <sup>4</sup>, and the corresponding sky coverage is from Figure 1 of B04. Note that they combined the CDF-N and CDF-S source catalogs and then derived the CDFs number counts. Using the cumulative CDFs number counts and their sky coverages, we derived the differential number counts of the CDFs in

---

<sup>4</sup>See <http://www.astro.psu.edu/users/niel/hdf/hdf-chandra.html>.

the 0.5-2 keV and 2-8 keV bands. Then, we simultaneously fitted the differential number counts of the ChaMP and the CDFs with a broken power law. In Figure 5, we display the differential and the cumulative number counts of the ChaMP+CDFs in the 0.5-2 and 2-8 keV bands. The best fit parameters are listed in Table 3 and displayed in Figure 5 as red lines. The ChaMP+CDFs number counts cover a flux range of  $2 \times 10^{-17} \sim 2.4 \times 10^{-12}$  (0.5-2 keV) and  $2 \times 10^{-16} \sim 7 \times 10^{-12}$  (2-8 keV)  $\text{erg cm}^{-2} \text{sec}^{-1}$ . The bright flux end of the ChaMP+CDFs and the faint flux end of the ChaMP agree well. Thus the number counts are well established with smaller statistical errors over a wide flux range.

Figure 6 compares the best fits to the differential number counts of the ChaMP alone with those of the ChaMP+CDFs. Overall, the ChaMP and the ChaMP+CDFs number counts agree within the uncertainties in the Sc and the Hc bands; however, in the Hc band, the faint power index  $\gamma_1$  of the ChaMP ( $1.83^{+0.16}_{-0.16}$ ) is steeper than that of the ChaMP+CDFs ( $1.59^{+0.13}_{-0.07}$ ) at  $1.2\sigma$  confidence. B04 investigated the number counts of the CDF-N and the CDF-S independently, as well as those of the combination of both CDFs, and found that in the Hc band the CDF-N is steeper than that of the CDF-S at flux fainter than  $10^{-15} \text{ erg cm}^{-2} \text{sec}^{-1}$  and this deviation increases to  $3.9\sigma$  at the faintest flux limits. They suggested that this is caused by field-to-field variations, as also reported by Cowie et al. (2002). Note that they did not find any significant evidence for field-to-field variations in the Hc band at fluxes brighter than  $10^{-15} \text{ erg cm}^{-2} \text{sec}^{-1}$ , or across the entire flux range of the Sc band as already reported by KD04 in the ChaMP study. Although the faint flux limit of the ChaMP number counts ( $\sim 2 \times 10^{-15} \text{ erg cm}^{-2} \text{sec}^{-1}$  in the Hc band) is brighter than that of the CDFs ( $\sim 2 \times 10^{-16}$ ), the large size of the ChaMP sample taken from 130 serendipitous *Chandra* fields provides the best estimate of the average number counts. Therefore, it is likely that the CDF-S contains fewer faint sources in the Hc band than the average number count distributions at  $\gtrsim 1.2\sigma$  confidence levels.

### 4.3. Comparison with Previous Studies

In this section, we compare the ChaMP and the ChaMP+CDFs number counts with those of previous studies. Table 4 provides the best fit parameters, the sky coverage, the faint and bright flux limits, the fitting space (in cumulative or differential spaces), and the fitting formula for each study. Figure 7 shows the number of sources and the sky coverage of various surveys. The largest sky coverage area is  $92 \text{ deg}^2$  and  $74 \text{ deg}^2$  in the soft and hard band, respectively, for the combination data of *ROSAT*, *Chandra*, and *XMM-Newton* surveys (M03). The ChaMP+CDFs covers the second largest sky area of  $9.8 \text{ deg}^2$ ; however, it contains the largest number of sources due to the better resolution and sensitivity of *Chandra* compared with other X-ray observatories. In Figure 8, we plot the faint and bright flux limits of this and previous studies. The ChaMP covers

the widest flux range in the broad band. In the soft and hard bands, M03 covers the widest flux ranges, although the ChaMP+CDFs also spans a very wide flux range. Overall, the ChaMP and the ChaMP+CDFs samples are second in sky area and flux range; however, they have the largest number of sources observed with a single satellite, *Chandra*.

The differential number counts can be described by a double power law (Cowie et al. 2002; Harrison et al. 2003; Yang et al. 2004; Basilakos et al. 2005; Chiappetti et al. 2005) or by a broken power law (Baldi et al. 2002; Kim, D.-W. et al. 2004b). Manners et al. (2003) fitted their differential number counts with a single power law. M03 introduced a fitting formula for the cumulative number counts which is a combination of two power laws (see equation (2) in M03), and they fitted their number counts in differential space as follows:

$$\frac{dN}{dS} = K(2 \times 10^{-15})^{\gamma_1} \left[ \frac{\gamma_1 S^{(\gamma_1-1)} + \gamma_2 S_b^{(\gamma_1-\gamma_2)} S^{(\gamma_2-1)}}{(S^{\gamma_1} + S_b^{(\gamma_1-\gamma_2)} S^{\gamma_2})^2} \right], \quad (6)$$

where  $\gamma_1$  and  $\gamma_2$  are the two power indices,  $K$  is a normalization factor, and  $S_b$  is the discontinuity in the cumulative number counts space. Therefore, we can not directly compare the exact parameters of equation (6) with those of a double power law or a broken power law.

In Figure 9, we compare the double or broken power law slopes of the differential number counts for this study with those for previous studies in the soft (*left panels*) and the hard (*right panels*) bands, respectively. In both soft and hard bands, the slopes at faint ( $\gamma_1$ ) and at bright ( $\gamma_2$ ) fluxes for the ChaMP+CDFs agree with those of previous studies within the uncertainties. We note that  $\gamma_2$  of the ChaMP+CDFs is slightly steeper than that for the previous ChaMP study (KD04) in which the hard band number counts was fitted by single power law only for the bright flux regime due to the shallow faint flux limit. In this study, in the hard band, the  $\gamma_1$  for the ChaMP is slightly steeper than that for Cowie et al. (2002), H03, and the ChaMP+CDFs. Overall, the ChaMP+CDFs number counts agree with those of previous studies within the uncertainties in the soft and hard bands and they present statistically robust number counts with the smallest uncertainties.

## 5. Break of the Differential Number Counts

### 5.1. Origin of Different Break Fluxes in Different Bands

In §4, we detected the break fluxes of the differential number counts in 6 energy bands and they have different flux levels in each energy band (see  $S_b$  in Table 3). The simplest explanation is that the break flux shifts as a function of energy band due to the corresponding flux levels in each band. To investigate this possibility, we estimate the flux shift by rescaling the break flux in a given energy band into the other energy bands using an assumed X-ray source spectrum. We assumed

a single power law model for the spectra for the X-ray sources, and estimated the expected break fluxes  $S_{b,exp}$  in each energy band relative to a given break flux  $S_{b,std}$  in a standard band as follows:

$$S_{b,exp}(E_1 - E_2) = S_{b,std} \frac{\int_{E_1}^{E_2} E^{-\Gamma_{ph}} E dE}{\int_{E_{S1}}^{E_{S2}} E^{-\Gamma_{ph}} E dE}, \quad (7)$$

where  $S_{b,std}$  is a break flux in a standard  $E_{S1} - E_{S2}$  keV energy band and  $\Gamma_{ph}$  is the photon index of a spectrum. To calculate the expected break fluxes of the ChaMP and the ChaMP+CDFs, we used  $S_{b,std} = 2.5 \times 10^{-14}$  and  $S_{b,std} = 2.2 \times 10^{-14} \text{ erg cm}^{-2} \text{ sec}^{-1}$  which are the measured break flux in the 0.3-8 keV band with a photon index of  $\Gamma_{ph} = 1.4$  and  $\Gamma_{ph} = 1.7$ , respectively.

In Figure 10, we compare the expected and measured break fluxes of the ChaMP, ChaMP+CDFs, and XMM-LSS (Chiappetti et al. 2005) number counts in several X-ray energy bands. For the XMM-LSS, the expected break flux is calculated by assuming a photon index of  $\Gamma_{ph} = 1.7$  and  $S_{b,std}$  is the measured break flux in the He (2-10 keV) band for consistency with their study. Overall, expected and measured break fluxes agree within the uncertainties. Since M03 fitted their differential number counts with a nonlinear equation (see equation (6)) rather than a broken or a double power law, we can not include their results. However, according to our own visual estimations, the break fluxes of their study also follow the trend in Figure 10. Therefore, we conclude that the break flux shifts as a function of energy band due to the corresponding flux levels in each band. Although we can not rule it out without detailed source classification, which is beyond the scope of this paper, there is no need to invoke a different population to explain the shift.

## 5.2. Cause of the Break

In §5.1, we found that different break flux levels in different energy bands could be explained by the identical X-ray population(s) in each energy band. Then, what causes the break flux? To answer this question, it is best to classify all X-ray sources using optical spectroscopy and then to investigate which population(s) is responsible for a break in their number counts. However, it is difficult to obtain optical spectra of X-ray sources: some X-ray sources have very faint or no optical counterparts. B04 classified their CDFs sources based on X-ray-to-optical flux ratio, optical spectrum, and X-ray properties such as X-ray spectrum and luminosity, and determined the number counts for X-ray populations such as AGNs, star forming galaxies, and Galactic stars. They classified AGNs in more detail, such as Type 1, Type 2, unobscured, and obscured AGNs, and they determined the number counts for each AGN subclass. However, the flux limits of the CDFs are not bright enough to investigate the origin of break fluxes.

The ChaMP is a multi-wavelength survey, including follow-up at optical, spectroscopic, IR, and radio wavelengths as well as matching with published catalogs such as SDSS and 2MASS.

Since these follow-up surveys are not yet completed, only part of the ChaMP sample can be classified on the basis of multi-wavelength properties. The follow-up surveys of the ChaMP are still on going and we will be able to investigate this issue in more detail by source classifications covering break flux regimes. Thus in this study we use only the X-ray properties such as the hardness ratio  $HR = (H_c - S_c) / (H_c + S_c)$  to investigate the cause of the break flux and include all ChaMP X-ray sources. The HR of the ChaMP sources was calculated by a Bayesian approach which models the detected counts as a Poisson distribution rather than a Gaussian distribution to successfully describe the statistical nature of the faint sources (Park et al. 2006; KM06).

### 5.2.1. Hardness Ratio and Break Flux

H03 constructed the differential number counts for the SEXSI sources in the 2-10 keV band divided into hard and soft sources at a hardness ratio of  $HR = 0$ . They found that the number counts for the soft ( $HR < 0$ ) sources show a break while the hard ( $HR > 0$ ) sources do not. They suggested that, on average, the hard sources may be at lower redshift, and so do not show the cosmological evolutionary effects which cause the break. Following H03, we investigated the HR dependence of the break flux for the ChaMP number counts in all energy bands.

The left panels of Figure 11 shows HR distributions of the ChaMP sources as a function of flux in 3 energy bands. The break fluxes ( $S_b$ ) reported in Table 3 of §4 are also plotted. In the right panels of Figure 11, we display the number distributions of the HR for sources in the following categories: all sources, sources fainter than the break flux ( $S < S_b$ ), and sources brighter than the break flux ( $S > S_b$ ). In all energy bands, there are fewer hard than soft sources at bright fluxes. We performed a Kolmogorov-Smirnov test (KS test, Press et al. 1992) to estimate the probability of faint and bright samples having the same hardness ratio distribution and it is significantly low ( $prob < 1 \times 10^{-10}$ ) in each energy band. Overall, most hard sources are distributed at  $S < S_b$ , while soft sources cover the entire flux range. Thus we defined samples at  $HR \leq 0$  in all energy bands to investigate the relation between the source HR and the break in the number counts. In §5.2.3, we investigate the flux-hardness ratio (S-HR) diagram in more detail by performing a simple simulation for a test X-ray source over a range of redshift and absorption to understand why bright, hard sources are rare in all energy bands.

In the left panels of Figure 12, we display the differential number counts for the soft ( $HR < 0$ ) and the hard ( $HR > 0$ ) sources in 3 energy bands. We fitted the soft sources with a broken power law and the hard sources with a single power law. The best fit parameters are listed in Table 5 and displayed in Figure 12 as red lines. In all energy bands, the differential number counts for soft sources show a break while those for hard sources do not. We performed a KS test (Press et al. 1992) for the flux distribution of the soft and hard sources, and there is no possibility that those

samples have the same flux distribution ( $prob < 4 \times 10^{-17}$ ) in each energy band. To statistically confirm the absence of the break in the hard source number counts, we also performed an F-test which is a model comparison test to select the best model from two competing models, a single and a broken power law. We used the *ftest* in the *Sherpa*<sup>5</sup> tool and a standard criterion of *ftest* for selecting the complex model is  $significance < 0.05$  (the 95% criterion of statistics). We fitted the hard source number counts with both a single and a broken power law and the broken power law model was rejected ( $significance > 6 \times 10^{-2}$ ) in all energy bands. We note that for the soft source number counts, the single power law model was rejected ( $significance < 5 \times 10^{-3}$ ) in all energy bands.

We note that the number of soft sources is larger than that of hard sources by a factor of  $\sim 10$  ( $\sim 2$ ) in the Sc (Hc) band (see Table 5), thus it is possible that the hard sources do not show the break due to small number statistics. To check this possibility, we produced 1,000 random subsets from the soft sources in each energy band: each subset has the same number of sources as the hard source samples. We derived the differential number counts for each subset and display their averaged differential number counts in the right panels of Figure 12. The error bar represents the averaged error from each differential number counts. We note that the statistical fluctuation for each random subset is comparable to the averaged error. Even with the reduced statistics, soft sources still show a detectable break. Thus smaller number of hard sources does not prevent detection of a break in our sample. Our results agree with those reported by H03 in the 2-10 keV band. Therefore, we conclude that the soft sources are responsible for the break in the differential number counts in all energy bands.

We compare the best fit parameters of the soft and the hard subsamples with those of the total sample which includes all sources regardless of HR (see §4 and Table 3). In Figure 13 (a)-(c), we compare the soft sample with the total sample: the faint power law indices are systematically shallower (at  $5.7\sigma$ ) than those of the total samples, while the bright power law indices and break fluxes agree well with those of the total samples, within the uncertainties. In Figure 13 (d), we compare the hard sample with the total sample: the hard band (H and Hc) indices are shallower (at  $2.6\sigma$ ) than those of the total samples, while the broad and soft band indices agree to within the uncertainties. To quantitatively estimate the slope changes which indicate the strength of the break, we introduce a break factor as follows:

$$BF \equiv (\gamma_2 - \gamma_1)/(\gamma_2 + \gamma_1), \quad (8)$$

where  $\gamma_1$  and  $\gamma_2$  are the faint and bright power indices of the differential number count (see equation (3)). As the strength of the break increases, the break factor increases. The break factors of the

---

<sup>5</sup>See <http://asc.harvard.edu/sherpa/threads/index.html>.

total and the soft sample are listed in Table 6. We found that the break factors tend to be smaller in the total samples than in soft samples for all energy bands, and that the break factors tend to be larger in the soft bands than in the hard bands.

### 5.2.2. *Redshift Distributions of Soft and Hard Sources*

Why do soft sources show a break while hard sources do not? H03 suggested that the hard sources may be predominantly at lower redshifts and so do not show the cosmological evolution effects which cause the break. To investigate this suggestion, we display the redshift distributions of the soft and hard sources in Figure 14. In our sample, 63 ChaMP fields were covered by optical follow-up survey and 669 out of 5515 sources have redshifts, of which we used the sources with  $S/N > 1.5$ , matching with optical sources at the highest confidence level, and having the highest confidence level of spectrum identification (for detail descriptions of the optical follow-up survey, spectroscopy and redshifts in the ChaMP, see Green et al. (2004) and Silverman et al. (2005)). In all energy bands, the hard sources distribute at lower redshifts than the soft sources. We performed a KS test (Press et al. 1992) to estimate the probability for soft and hard sources having the same redshift distribution and it is significantly low ( $prob < 1 \times 10^{-4}$ ) in each energy band.

Since the spectroscopy of the ChaMP sources was biased toward optically bright sources, this bias may affect the X-ray source selection for measuring redshifts and may cause the lower redshift distribution of hard sources: more soft than hard sources selectively have redshifts. In the top panel of Figure 15, we display the hardness ratio distributions of the ChaMP sources in the B (0.3-8 keV) band in the following categories: all sources, sources with optical imaging observations in 63 ChaMP fields, sources having an optical counterpart, and sources having a redshift. In the bottom panel of Figure 15, we display the number ratios of the last three subsamples over total sample in each hardness ratio bin. Overall, 60% of sources were covered by the optical follow-up survey, of those, 32% of sources have an optical counterpart, and of those, 5% of sources have a redshift. The fraction of sources having a redshift is  $5.2 \pm 2\%$  for soft sources and  $6.7 \pm 6\%$  for hard sources, respectively. Thus, the bright source selection in the optical band does not significantly affect the X-ray source selection for measuring redshift as a function of hardness ratio.

Then, why are hard sources distributed at lower redshifts? Since the QE and the effective area of the *Chandra* ACIS are lower and smaller in the hard band <sup>6</sup>, and the X-ray source counts are fewer in the hard band than in the soft band when a power law spectrum is assumed, it is possible to miss more hard sources than soft sources especially at higher redshift. Also, it is possible that

---

<sup>6</sup>See Chapter 6 of the *Chandra* Proposers' Observatory Guide Rev.8.0.

an intrinsically hard source may be observed as a soft source due to the cosmological redshift. In §5.2.3, we quantitatively investigate this issue in more detail.

### 5.2.3. Redshift and Absorption Effects on X-ray Properties

To understand the dependence of X-ray properties, such as flux and hardness ratio, on the redshift and absorption, we performed a simple simulation for a test X-ray source using the *Sherpa*<sup>7</sup> tool. We assumed a power law model spectrum for the test X-ray source as follows:

$$F(E) = K(E \times (1+z)/(1\text{keV}))^{-\Gamma_{ph}}, \quad (9)$$

where  $z$  is a redshift and  $\Gamma_{ph}$  is a photon index of the test X-ray source.  $K$  is a normalization constant at 1 keV in units of  $\text{photons keV}^{-1} \text{ cm}^{-2} \text{ sec}^{-1}$  and we set  $K = 0.5$ . We assumed a Galactic absorption and intrinsic absorption using Wisconsin cross-sections (Morrison & McCammon 1983) as follows:

$$A(E) = \exp(-N_{H,Gal} \times \sigma(E)), \quad (10)$$

$$A(E) = \exp(-N_{H,int} \times \sigma(E \times (1+z))), \quad (11)$$

where  $\sigma(E)$  is the photo-electric cross-section not including Thomson scattering and  $z$  is the redshift.  $N_{H,Gal}$  and  $N_{H,int}$  are equivalent hydrogen column density in units of  $\text{atoms cm}^{-2}$  for the Galactic and intrinsic absorption, respectively. We selected a ChaMP ACIS-I observation whose Galactic absorption is  $N_{H,Gal} = 1.18 \times 10^{20} \text{ cm}^{-2}$ . Using the ancillary response function (ARF) and redistribution matrix function (RMF) files, we calculated the source flux and hardness ratio at the aim point for various ranges of redshift ( $0 \leq z \leq 10$ ) and intrinsic absorption ( $10^{20} \leq N_{H,int} \leq 10^{24} \text{ cm}^{-2}$ ).

In Figure 16, we display the flux-hardness ratio (S-HR) diagram in 3 energy bands. All ChaMP sources with  $S/N > 0$  are displayed and the grid indicates the predicted location of a test source with various redshifts ( $z = 0, 1, 2$ , and  $3$ ) and intrinsic absorption column densities ( $\log N_{H,int} = 20, 21.7, 22, 22.7$ , and  $23.7$ ). A photon index of  $\Gamma_{ph} = 1.4$  was assumed for the test source spectrum. We note that the flux of grid was renormalized to be displayed with the ChaMP scatter plot. The source becomes fainter with increasing absorption and with increasing redshift. The source becomes harder with increasing intrinsic absorption, but softer with increasing redshift. In the soft band (0.5-2 keV), this effect is more significant than in the hard and broad bands. From this ideal case study, we can understand the observed flux-hardness ratio diagram in which there are fewer bright hard sources in each energy band (see §5.2.1). The test X-ray source does not cover

---

<sup>7</sup>See <http://asc.harvard.edu/sherpa/threads/index.html>.



the region  $HR \leq -0.4$ ; but will cover this regime when a steeper power law index (i.e.,  $\Gamma_{ph} > 2$ ) is assumed (see Figure 17).

Figure 17 shows the hardness ratio of the test X-ray source as a function of redshift with a range of intrinsic absorption ( $20 \leq \log N_{H,int} \leq 24$ ) for different photon indices. The test source with steeper power index (i.e.,  $\Gamma_{ph} = 2$  and 3) covers the soft hardness regime ( $HR \leq -0.5$ ). Again, the test source becomes harder with increasing intrinsic absorption; but, softer with increasing redshift. For example, in the top left panel (assumed  $\Gamma_{ph} = 1.4$ ), the hard source with  $\log N_H = 22$  is not observed as a hard source anymore even at  $z \sim 1$ , and most hard sources are observed as soft sources at  $z > 3$ . Therefore, a hard source with high redshift is observed as a soft source in the observed frame due to the cosmological redshift, and so hard sources with high redshifts are rare (§5.2.2). Thus the hard source number counts do not include high redshift hard sources, while the soft source number counts include both intrinsically hard and soft sources.

In §5.2, we found that the hard sources do not show a break in their number count distributions and distribute at lower redshifts compared to soft sources. The soft sources show the break in their number count distributions, and distribute from low to high redshifts (see Figure 12 and 14). The observed soft sources may be a mixture of soft sources and redshifted hard sources (see Figure 17). These results likely support the suggestion that the hard sources may be preferentially at lower redshifts, and so do not show cosmological evolution effects (H03). In addition to H03's suggestion, we suggest that the break in the soft source number counts may be caused by the mixture of X-ray source populations as well as cosmological evolution effects. To investigate this suggestion, we need redshifts/classifications of the X-ray sources. Since it is not possible to speculate on the distribution of properties such as intrinsic absorption  $N_{H,int}$  from the source counts alone, we need to assume a model for the  $N_{H,int}$  distribution of X-ray point sources as a function of redshift and luminosity or perform X-ray spectral analysis. B04 found that the source density of Type 1 AGNs is 10-20 times lower than that of Type 2 AGNs at the CDF flux limits in both of the 0.5-2 keV and 2-8 keV bands. Also, they found that the source density of unobscured/mildly obscured AGNs is 2-3 times lower than those of obscured AGNs at the CDF limits. La Franca et al. (2005) found that the fraction of absorbed ( $N_H > 10^{22} \text{ cm}^{-2}$ ) AGNs decreases with intrinsic X-ray luminosity but increases with redshift. The fraction of Type 1/Type 2 AGN (absorbed/unabsorbed AGN) probably affects the break in the differential number counts. Also, since the hard band is less affected by absorption than the soft band, it is possible that the strength of the break is related to the fraction of absorbed sources in each energy band. We expect that further studies can be performed using the ChaMP data once we have more optical/spectroscopy follow-up observations.

## 6. Cosmic X-ray Background

### 6.1. Resolved Cosmic X-ray Background Flux Density

The contribution of discrete sources to the CXRB flux density can be calculated from the differential number counts as follows (M03):

$$F_{resol} = \int_{S_{faint}}^{S_{bright}} \left( \frac{dN}{dS} \right) S' dS', \quad (12)$$

where  $S_{faint}$  and  $S_{bright}$  are the faint and bright flux limits of the sample.

The ChaMP is a serendipitous *Chandra* archival survey, therefore most observations contain target sources as intended by the PI and which have brighter flux than non-target sources as shown in Figure 18. To avoid biased source selection, we excluded target sources for deriving the ChaMP and the ChaMP+CDFs number counts. Even though we have only 85 target sources in total, their contributions to the CXRB flux density are not negligible because of their brightness (M03). Thus we need to correct the bright target source contributions to the CXRB. Since the target sources cover a relatively wide flux range,  $3 \times 10^{-16} \sim 7 \times 10^{-13}$  (0.5-2 keV) and  $2 \times 10^{-14} \sim 2 \times 10^{-12}$  (2-8 keV)  $erg\ cm^{-2}\ sec^{-1}$ , respectively, we can not simply adapt the bright part of the number counts for full sky surveys such as *ROSAT All Sky Survey* (soft band) or *HEAO-1 A2* extra galactic survey (hard band) that were used by M03 to correct their bright target source contributions to the CXRB. Therefore, we present the lower and upper limits of the resolved CXRB flux density from the ChaMP and ChaMP+CDFs number counts by excluding target sources and including target sources, respectively. We derived again the ChaMP and the ChaMP+CDFs number counts including target sources and list their best fit parameters in Table 7. Comparing with the best fit parameters without target sources (Table 3), target sources make the bright power law indices ( $\gamma_2$ ) shallower at  $0.9\sigma$  confidence, while the faint power law indices ( $\gamma_1$ ) and break fluxes ( $S_b$ ) show differences at  $0.5\sigma$  and  $0.3\sigma$ , respectively.

Table 8 lists the resolved CXRB flux densities and their contributions to the total CXRB from the ChaMP and the ChaMP+CDFs when the target sources are excluded or included in 6 energy bands. The average total CXRB flux densities of  $(7.52 \pm 0.35) \times 10^{-12}$  (0.5-2 keV) and of  $(1.79 \pm 0.11) \times 10^{-11}$  (2-8 keV)  $erg\ cm^{-2}\ sec^{-1}\ deg^{-2}$  (B04) are assumed. In the Bc band, the total CXRB flux density is the sum of those in the Sc and Hc bands. The total CXRB flux density in the B, S, and H bands are rescaled from the Bc, Sc, and Hc bands, respectively, by assuming a photon index of  $\Gamma_{ph} = 1.4$ . In Figure 19, we display the resolved CXRB flux density calculated from the ChaMP+CDFs as a function of flux limit in the Sc and Hc bands, respectively. We plot the resolved CXRB flux densities calculated from the differential number counts with (*blue lines*) and without (*red lines*) target sources. The ChaMP sources resolve the total CXRB without (with) target sources at  $80 \pm 2$  ( $86 \pm 2\%$ ) and  $72 \pm 2$  ( $76 \pm 2\%$ ) in the Sc and Hc bands,

respectively. Since the ChaMP+CDFs covers wider flux range than the ChaMP, the ChaMP+CDFs sources resolve more total CXRB by up to  $4 \sim 7\%$  in each band. We extrapolated the best fit ChaMP+CDFs number counts without target sources down to  $10^{-20} \text{ erg cm}^{-2} \text{ sec}^{-1}$  and found that the total CXRB is not fully resolved in the soft and hard energy bands within the uncertainties. We note that for the 2-8 keV band, extrapolating the best fit ChaMP+CDFs number counts with target sources down to  $\sim 10^{-17} \text{ erg cm}^{-2} \text{ sec}^{-1}$ , the total CXRB flux density is fully resolved within the large uncertainties. In Figure 20, we display the difference between the resolved CXRB excluding and including target sources, normalizing with that of excluding targets. At bright flux limits, the flux density differences are up to 100%; however, at faint flux limits, the differences are less than 10% in each energy band. The resolved CXRB with and without target sources are upper and lower limits of the resolved CXRB, respectively, and the actual resolved CXRB is between those values. In all energy bands, the fractions of the resolved CXRB increase by  $5 \sim 6\%$  when target sources are included.

In Figure 21, we display the resolved CXRB flux density (*top*) and the fraction of resolved CXRB (*bottom*) as a function of faint flux limit in each energy band. Excluding bright target sources, M03 estimated the resolved CXRB flux densities to be  $0.69^{+0.03}_{-0.02} \times 10^{-11}$  (0.5-2 keV) and  $1.40^{+0.09}_{-0.08} \times 10^{-11}$  (2-8 keV, rescaled from that in the 2-10 keV band assuming a photon index of  $\Gamma_{ph} = 1.4$ )  $\text{erg cm}^{-2} \text{ sec}^{-1} \text{ deg}^{-2}$ , respectively. From the ChaMP+CDFs without target sources, we estimated the resolved CXRB flux density to be  $0.63^{+0.01}_{-0.01} \times 10^{-11}$  (0.5-2 keV), lower than that of M03 at  $2\sigma$  level, and  $1.40^{+0.03}_{-0.03} \times 10^{-11}$  (2-8 keV)  $\text{erg cm}^{-2} \text{ sec}^{-1} \text{ deg}^{-2}$  in good agreement with M03, respectively. The fractional contributions of the ChaMP+CDFs X-ray point sources excluding (including) target sources to the total CXRB are  $84 \pm 2(91 \pm 2)\%$  and  $78 \pm 2(84 \pm 4)\%$  in the Sc and Hc band, respectively.

## 6.2. Total Cosmic X-ray Background Flux Density

In §6.1 we used the measured total CXRB flux density (B04); however, we can also derive the total CXRB flux density from the sum of resolved and unresolved components, using the resolved CXRB estimated from the ChaMP+CDFs. Recently, HM06 measured unresolved CXRB flux densities using the *Chandra* Deep Fields North and South of  $(0.18 \pm 0.03) \times 10^{-11}$ ,  $(0.34 \pm 0.17) \times 10^{-11}$ , and  $(0.10 \pm 0.01) \times 10^{-11} \text{ erg cm}^{-2} \text{ sec}^{-1} \text{ deg}^{-2}$  in the 0.5-2 keV, 2-8 keV, and 1-2 keV bands, respectively, after removing all detected point and extended sources in those fields. They also estimated the resolved CXRB flux densities from the CDFs, and from the *ROSAT* (0.5-2 keV, Vikhlinin et al. (1995)) and the *Chandra*, XMM, and ASCA (2-10 keV, M03) for the flux ranges brighter than CDFs. And then, they derived the total CXRB flux densities by adding those resolved and unresolved components.

We derive the total CXRB by adding HM06’s unresolved CXRB values to the resolved CXRB of the ChaMP+CDFs. Since these are estimated from a single satellite, *Chandra*, there are no cross-calibration uncertainties as in multiple satellite data. In Table 9, we list the resolved, unresolved, and total CXRB flux densities estimated from this and previous studies. For this study, the resolved CXRB in the 1-2 keV band was rescaled from that in the 0.5-2 keV assuming a photon index of  $\Gamma_{ph} = 1.4$ . We also provide the total CXRB with and without target sources, which gives lower and upper limits to the total CXRB, respectively. The actual total CXRB is between these two values. The total CXRB flux densities increase by  $\sim 6\%$  when target sources are included. Our results agree well with those of HM06 but are lower than earlier numbers,  $\sim 80\%$  compared with 90 – 94% (M03; B04, see Table 9). Given the large uncertainties in the M03 and B04 studies, they remain marginally consistent ( $\sim 2\sigma$  differences).

We note that, in this study, the total CXRBs include two kinds of unquoted uncertainty. First, the total CXRBs could be overestimated due to the incompleteness correction. The number counts are corrected for incompleteness; however, this corrected portion may be also included in the unresolved CXRB since they are not resolved in the observations. Our resolved CXRBs were corrected for incompleteness by 7% (0.5-2 keV)  $\sim$  18% (2-8 keV); however, since HM06 used only the central  $5'$  around each CDF pointing in which the count recovery rate and the detection probability of the source are higher than those at the off-axis region (B04; KM06), the duplicated fraction of the total CXRB is much smaller than the corrected fraction. Second, the total CXRBs could be underestimated since we do not include the resolved CXRB that originates from X-ray extended sources. The resolved CXRB from the *ROSAT* deep cluster survey in the flux range of  $10^{-14} \sim 10^{-11} \text{ erg cm}^{-2} \text{ sec}^{-1}$  (Rosati et al. 1998) increases our total CXRB flux density by up to 10%, and their contribution to the total CXRB will be 9.5% in the 0.5-2 keV band. We note that, with this extended source contribution, our total CXRB still agrees with that of other studies within the uncertainties. Meanwhile, so far, there are no number counts for X-ray extended sources in the hard band. Since the spectrum of an extended source is not a simple power law, we can not rescale the resolved CXRB in the soft band to that in the hard band. Thus, we did not include the extended source contribution to the total CXRB in all energy bands. Since the ChaMP includes extended sources as well (Barkhouse et al. 2006), in a future ChaMP study we expect to determine their number counts both in the soft and the hard bands with higher confidence levels by performing extensive simulations to accurately correct their incompleteness. Then, we will be able to estimate the resolved CXRB for extended sources, giving us a self-consistent total CXRB flux density from *Chandra*.

## 7. Summary and Conclusions

We present the *Chandra* Multiwavelength Project (ChaMP) X-ray point source number counts in 6 energy bands. We also present the ChaMP+CDFs number counts in the 0.5-2 keV and 2-8 keV which covers large flux ranges with small statistical errors. Using these number counts, we measure the resolved and total CXRB flux densities in multiple X-ray energy bands. The main results and conclusions of this study are the following.

1. The number counts of the ChaMP and the ChaMP+CDFs are well fitted with a broken power law. The best fit faint and bright power indices of the ChaMP+CDFs are  $1.49^{+0.02}_{-0.02}$  and  $2.36^{+0.05}_{-0.05}$  (0.5-2 keV),  $1.58^{+0.01}_{-0.01}$  and  $2.59^{+0.06}_{-0.05}$  (2-8 keV), respectively. The number counts in this study agree with those of previous studies within the uncertainties but are better constrained.

2. In all energy bands, we detect a break in the differential number counts which is a function of energy band. The origin of the break depending on energy band can be explained by the identical X-ray population(s) in each energy band.

3. In all energy bands, the soft sources are responsible for the break in the differential number counts. A hard X-ray source becomes softer with increasing redshift, and so the hard source number counts do not include high redshift sources while the soft source number counts include both soft sources with full range of redshifts and intrinsically hard sources with high redshifts. Therefore, the soft sources show the break due to the cosmological evolutionary effects and mixture of X-ray populations.

4. The resolved CXRB flux densities are measured from the ChaMP and the ChaMP+CDFs number counts in multiple energy bands. We present upper and lower limits of the resolved CXRB by estimating with and without bright target sources.

5. Excluding target sources, the total CXRB flux densities in units of  $\text{erg cm}^{-2} \text{sec}^{-1} \text{deg}^{-2}$  are  $0.81^{+0.03}_{-0.03} \times 10^{-11}$  (0.5-2 keV),  $1.74^{+0.17}_{-0.17} \times 10^{-11}$  (2-8 keV), and  $0.48^{+0.02}_{-0.02} \times 10^{-11}$  (1-2 keV), respectively. Including target sources, the total CXRB flux densities in units of  $\text{erg cm}^{-2} \text{sec}^{-1} \text{deg}^{-2}$  are  $0.86^{+0.03}_{-0.03} \times 10^{-11}$  (0.5-2 keV),  $1.84^{+0.18}_{-0.18} \times 10^{-11}$  (2-8 keV), and  $0.51^{+0.02}_{-0.02} \times 10^{-11}$  (1-2 keV), respectively.

6. When the total CXRB estimated from this study is assumed in each band, excluding target sources, the resolved CXRB fractions are  $78.1^{+1.2}_{-1.2}\%$  (0.5-2 keV),  $80.5^{+1.7}_{-1.7}\%$  (2-8 keV),  $78.5^{+1.2}_{-1.2}\%$  (1-2 keV), respectively. Including target sources, the resolved CXRB fractions are  $79.3^{+1.2}_{-1.2}\%$  (0.5-2 keV),  $81.5^{+3.8}_{-3.8}\%$  (2-8 keV), and  $79.8^{+1.2}_{-1.2}\%$  (1-2 keV), respectively.

We gratefully acknowledge support for this project under NASA CXC archival research grant AR4-5017X and AR6-7020X . PJG, DWK, HT, and BJW also acknowledge support through NASA Contract NAS8-03060 (CXC). MGL is in part supported by the KOSEF grant (R01-2004-

000-10490-0).

## REFERENCES

- Baldi, A., Molendi, S., Comastri, A., Fiore, F., Matt, G., & Vignali, C. 2002, *ApJ*, 564, 190
- Barkhouse, W. A., Green, P. J., Vikhlinin, A., Kim, D.-W., Perley, D., Cameron, R., Silverman, J., Mossman, A., Burenin, R., Jannuzi, B. T., Kim, M., Smith, M. G., Smith, R. C., Tananbaum, H., & Wilkes, B. J. 2006, *astro-ph/0603521*, accepted to *ApJ*
- Basilakos, S., Plionis, M., Georgakakis, A., & Georgantopoulos, I. 2005, *MNRAS*, 356, 183
- Bauer, F. E., Alexander, D. M., Brandt, W. N., Schneider, D. P., Treister, E., Hornschemeier, A. E., Garmire, G. P. 2004, *AJ*, 128, 2048 (B04)
- Brandt, W. N. & Hasinger, G., 2005, *ARA&A*, 43, 827
- Cappelluti, N., Cappi, M., Dadina, M., Malaguti, G., Branchesi, M., D’Elia, V., & Palumbo, G. G. C. 2005, *A&A*, 430, 39
- Cash, W. 1979, *ApJ*, 228, 939
- Cowie, L. L., Garmire, G. P., Bautz, M. W., Barger, A. J., Brandt, W. N., & Hornschemeier, A. E. 2002, *ApJ*, 566, L5
- Chiappetti, L., Tajer, M., Trinchieri, G., Maccagni, D., Maraschi, L., Paiono, L., Pierre, M., Surdej, J., Garcet, O., Gosset, E., Le Fvre, O., Bertin, E., McCracken, H. J., Mellier, Y., Foucaud, S., Radovich, M., Ripepi, V., Arnaboldi, M. 2005, *A&A*, 439, 413
- De Luca, A., & Moldendi, S. 2004, *A&A*, 419, 837
- Gehrels, N., et al. 1986, *ApJ*, 303, 336
- Gendreau, K. C., Barcons, X., & Fabian, A. C. 1998, *MNRAS*, 297, 41
- Green, P. J., Silverman, J. D., Cameron, R. A., Kim, D.-W., Wilkes, B. J., Barkhouse, W. A., LaCluyz, A., Morris, D., Mossman, A., Ghosh, H., Grimes, J. P., Jannuzi, B. T., Tananbaum, H., Aldcroft, T. L., Baldwin, J. A., Chaffee, F. H., Dey, A., Dosaj, A., Evans, N. R., Fan, X., Foltz, C., Gaetz, T., Hooper, E. J., Kashyap, V. L., Mathur, S., McGarry, M. B., Romero-Colmenero, E., Smith, M. G., Smith, P. S., Smith, R. C., Torres, G., Vikhlinin, A., Wik, D. R. 2004, *ApJS*, 150, 43

- Harrison, F. A., Eckart, M. E., Mao, P. H., Helefang, D. J., & Stern, D. 2003, *ApJ*, 596, 944 (H03)
- Hasinger, G., Burg, R., Giacconi, R., Hartner, G., Schmidt, M., Trumper, J., Zamorani, G. 1993, *A&A*, 275, 1
- Hickox, R. C., & Markevitch, M. 2006, *ApJ*, 645, 95 (HM06)
- Johnson, O., Best, P. N., & Almaini, O. 2003, *MNRAS*, 343, 924
- Kenter, A. & Murray, S. 2003, *ApJ*, 584, 1016
- Kim, D.-W., & Fabbiano, G. 2003, *ApJ*, 586, 826
- Kim, D.-W., Cameron, R. A., Drake, J. J., Evans, N. R., Freeman, P., Gaetz, T. J., Ghosh, H., Green, P. J., Harnden, F. R., Jr., Karovska, M., Kashyap, V., Maksym, P. W., Ratzlaff, P. W., Schlegel, E. M., Silverman, J. D., Tananbaum, H. D., Vikhlinin, A. A., Wilkes, B. J., & Grimes, J. P. 2004a, *ApJS*, 150, 19
- Kim, D.-W., Wilkes, B. J., Green, P. J., Cameron, R. A., Drake, J. J., Evans, N. R., Freeman, P., Gaetz, T. J., Ghosh, H., Harnden, F. R., Jr., Karovska, M., Kashyap, V., Maksym, P. W., Ratzlaff, P. W., Schlegel, E. M., Silverman, J. D., Tananbaum, H. D., & Vikhlinin, A. A. 2004b, *ApJ*, 600, 59 (KD04)
- Kim, E. et al. 2006, in preparation
- Kim, M. et al. 2006, submitted to *ApJS* (KM06)
- Kushino, A., Ishisaki, Y., Morita, U., Yamasaki, N. Y., Ishida, M., Ohashi, T., Ueda, Y. 2002, *Publ. Astron. Soc. Japan*, 54, 327
- La Franca, F., Fiore, F., Comastri, A., Perola, G. C., Sacchi, N., Brusa, M., Cocchia, F., Feruglio, C., Matt, G., Vignali, C., Carangelo, N., Ciliegi, P., Lamastra, A., Maiolino, R., Mignoli, M., Molendi, S., Puccetti, S. 2005, *ApJ*, 635, 864
- Lumb, D. H., Warwick, R. S., Page, M., & De Luca, A. 2002, *A&A*, 389, 93
- Manners, J. C., Johnson, O., Almaini, O., Willott, C. J., Gonzalez-Solares, E., Lawrence, A., Mann, R. G., Perez-Fournon, I., Dunlop, J. S., McMahon, R. G., Oliver, S. J., Rowan-Robinson, M., Serjeant, S. 2003, *MNRAS*, 343, 293
- Markevitch, M., Bautz, M. W., Biller, B., Butt, Y., Edgar, R., Gaetz, T., Garmire, G., Grant, C. E., Green, P., Juda, M., Plucinsky, P. P., Schwartz, D., Smith, R., Vikhlinin, A., Virani, S., Wargelin, B. J., Wolk, S. 2003, *ApJ*, 583, 70

- Moretti, A., Campana, S., Lazzati, D., & Tagliaferri, G. 2003, *ApJ*, 588, 696 (M03)
- Morrison, R.; McCammon, D. 1983, *ApJ*, 270, 119
- Murdoch, H. S., Crawford, D. F., & Janucey, D. L. 1973, *ApJ*, 183, 1
- Mushotzky, R. F., Cowie, L. L., Barger, A. J., & Arnaud, K. A. 2000, *Nature*, 404, 459
- Park, T., Kashyap, V. L., Siemiginowska, A., van Dyk, D. A., Zezas, A., Heinke, C., Wargelin, B. J. 2006, astro-ph/0606247, accepted to *ApJ*
- Parmer, A. N., Guainazzi, M., Oosterbroek T., Orr, A., Favata, F., Lumb, D., & Malizia, A. 1999, *A&A*, 345, 611
- Press, W. H., Teukolsky, S. A., Vetterling, W. T., Flannery, B. P 1992, *Numerical Recipes in Fortran*, Cambridge University Press
- Rosati, P., Tozzi, P., Giacconi, R., Gilli, R., Hasinger, G., Kewley, L., Mainieri, V., Nonino, M., Norman, C., Szokoly, G., Wang, J. X., Zirm, A., Bergeron, J., Borgani, S., Gilmozzi, R., Grogin, N., Koekemoer, A., Schreier, E., Zheng, W. 2002, *ApJ*, 566, 667
- Rosati, P., Della Ceca, R., Norman, C., & Giacconi, R. 1998, *ApJ*, 492, 21
- Silverman, J., Green, P., Barkhouse, W., Kim, D.-W., Aldcroft, T., Cameron, R., Wilkes, B., Mossman, A., Ghosh, H., Tananbaum, H., Smith, M., Smith, R., Smith, P., Foltz, C., Wik, D., Jannuzi, B. 2005, *ApJ*, 618, 123
- Stark, A. A., Gammie, C. F., Wilson, R. W., Bally, J., Linke, R. A., Heiles, C., Hurwitz, M. 1992, *ApJS*, 79, 77
- Tozzi, P., Gilli, R., Mainieri, V., Norman, C., Risaliti, G., Rosati, P., Bergeron, J., Borgani, S., Giacconi, R., Hasinger, G., Nonino, M., Streblyanska, A., Szokoly, G., Wang, J. X., & Zheng, W. 2006, *A&A*, 451, 457
- Vikhlinin, A., Forman, W., Jones, C., & Murray, S. 1995, *ApJ*, 451, 553
- Worsley, M. A., Fabian, A. C., Bauer, F. E., Alexander, D. M., Hasinger, G., Mateos, S., Brunner, H., Brandt, W. N., & Schneider, D. P., 2005, *MNRAS*, 357, 1281
- Yang, Y., Mushotzky, R. F., Steffan, A. T., Barger, A. J., & Cowie, L. L. 2004, *AJ*, 128, 1501



Table 1. Definition of Energy Bands

Range	Band	Definition
Broad	B	0.3-8 keV
	Bc	0.5-8 keV
Soft	S	0.3-2.5 keV
	Sc	0.5-2 keV
	Ss <sup>a</sup>	1-2 keV
Hard	H	2.5-8 keV
	Hc	2-8 keV
	He <sup>b</sup>	2-10 keV

<sup>a</sup>The Ss (2-10 keV) band was used only for estimating the CXRB flux density (see §6).

<sup>b</sup>The He (2-10 keV) band was not used in this study; however, it is referred for previous studies.

Table 2. Statistical Properties of X-ray Point Sources

	Band	Number	Min	Max	Median	Mean
	(1)	(2)	(3)	(4)	(5)	(6)
Count <sup>a</sup>	B	5515	5.42	40535.59	22.57	69.53
	S	4864	5.42	38117.52	19.24	61.50
	H	2575	5.41	11604.93	12.73	28.63
	Bc	5229	6.46	39760.98	23.46	70.52
	Sc	4554	5.41	36010.96	18.24	57.59
	Hc	3078	5.42	13624.92	13.72	31.63
Flux <sup>b</sup>	B	5515	0.63	7175.62	9.09	25.97
	S	4864	0.33	3286.49	4.36	12.78
	H	2575	1.27	6690.72	8.61	21.40
	Bc	5229	0.69	6767.74	9.04	25.38
	Sc	4554	0.26	2395.21	3.21	9.32
	Hc	3078	1.17	7112.31	8.87	21.88

Note. — Col. (1): X-ray energy band (see Table 1). Col. (2): number of sources. Col. (3): minimum value of the sample. Col. (4): maximum value of the sample. Col. (5): median value of the sample. Col. (6): mean value of the sample.

<sup>a</sup>Source net counts.

<sup>b</sup>Source flux with  $\Gamma_{ph} = 1.4$  in units of  $10^{-15} \text{ erg cm}^{-2} \text{ sec}^{-1}$ .

Table 3. List of the Best Fit Parameters without Target Objects

DATA	$\Gamma_{ph}$	Band	$K$	$\gamma_1$	$\gamma_2$	$S_b$
(1)	(2)	(3)	(4)	(5)	(6)	(7)
ChaMP	1.4	S	$769^{+14}_{-14}$	$1.57^{+0.01}_{-0.01}$	$2.41^{+0.05}_{-0.05}$	$9.9^{+0.7}_{-1.6}$
		H	$1828^{+48}_{-43}$	$1.81^{+0.01}_{-0.01}$	$2.58^{+0.05}_{-0.05}$	$14.2^{+0.9}_{-1.1}$
		B	$1614^{+28}_{-43}$	$1.65^{+0.01}_{-0.01}$	$2.44^{+0.06}_{-0.05}$	$25.0^{+1.9}_{-1.9}$
	1.7	S	$783^{+15}_{-15}$	$1.58^{+0.01}_{-0.01}$	$2.42^{+0.05}_{-0.05}$	$10.5^{+0.8}_{-0.8}$
		H	$1774^{+44}_{-41}$	$1.80^{+0.01}_{-0.01}$	$2.58^{+0.05}_{-0.05}$	$13.5^{+0.9}_{-0.9}$
		B	$1505^{+25}_{-41}$	$1.65^{+0.01}_{-0.01}$	$2.45^{+0.06}_{-0.05}$	$21.9^{+1.7}_{-1.7}$
	1.4	Sc	$607^{+12}_{-12}$	$1.54^{+0.02}_{-0.02}$	$2.36^{+0.05}_{-0.05}$	$6.8^{+0.5}_{-0.5}$
		Hc	$2040^{+50}_{-50}$	$1.82^{+0.01}_{-0.01}$	$2.65^{+0.07}_{-0.07}$	$19.2^{+6.3}_{-1.8}$
		Bc	$1557^{+28}_{-50}$	$1.64^{+0.01}_{-0.01}$	$2.48^{+0.05}_{-0.05}$	$22.9^{+1.6}_{-1.6}$
	1.7	Sc	$612^{+12}_{-12}$	$1.53^{+0.02}_{-0.02}$	$2.36^{+0.05}_{-0.04}$	$6.7^{+0.5}_{-0.5}$
		Hc	$1932^{+46}_{-48}$	$1.82^{+0.01}_{-0.01}$	$2.64^{+0.07}_{-0.07}$	$17.8^{+4.4}_{-1.7}$
		Bc	$1407^{+25}_{-48}$	$1.64^{+0.01}_{-0.01}$	$2.48^{+0.05}_{-0.05}$	$19.2^{+1.3}_{-1.4}$
ChaMP+	1.4	Sc	$571^{+11}_{-11}$	$1.49^{+0.02}_{-0.02}$	$2.36^{+0.05}_{-0.05}$	$6.5^{+0.4}_{-0.4}$
CDFs		Hc	$1258^{+29}_{-29}$	$1.58^{+0.01}_{-0.01}$	$2.59^{+0.06}_{-0.05}$	$14.4^{+0.9}_{-0.9}$

Note. — Col. (1): used data set. Col. (2): assumed photon index. Col. (3): X-ray energy band (see Table 1). Col. (4): normalization constant. Col. (5): faint power index of a broken power law. Col. (6): bright power index of a broken power law. Col. (7): break flux in units of  $10^{-15} \text{ erg cm}^{-2} \text{ sec}^{-1}$ .

Table 4. List of Fitting Parameters of Other Studies, ChaMP, and ChaMP+CDFs

Data (1)	Area (2)	Band (3)	$\Gamma_{ph}$ (4)	Number (5)	$K$ (6)	$S_{ref}$ (7)	$\gamma_1$ (8)	$\gamma_2$ (9)	$S_b$ (10)	$f_{min}$ (11)	$f_{max}$ (12)	FS (13)	FM (14)	Reference (15)
SSA13	0.03	0.5–2 2–10	1.4 1.2	22 15	185 170	7 20	$0.7 \pm 0.2$ $1.05 \pm 0.35$			0.23 2.5	7 20	C C	S S	Mushotzky et al. (2000)
HELLAS2XMM	3	0.5–2 0.5–2 2–10 5–10	1.7 1.7 1.7 1.7	1022 1022 495 100	$80.8^{+6.4}_{-5.3}$ $229^{+29.3}_{-19.6}$ $175.2^{+56.3}_{-36.2}$	10	$1.1 \sim 1.7$ $0.93 \pm 0.05$ $1.34^{+0.11}_{-0.10}$ $1.54^{+0.25}_{-0.19}$	$2.2^{+0.06}_{-0.09}$	$5 \sim 6.5$	0.59 0.59 2.8 6.2	500 500 6000 1000	D C C C	B S S S	Baldi et al. (2002)
CDFs+ SSA13/SSA22	0.25	2–8	1.2	373	$32 \pm 2$ $39 \pm 5$	10 10	$1.63 \pm 0.05$	$2.57 \pm 0.22$	12 12	0.2 0.2	100 100	D D	D D	Cowie et al. (2002)
CDF-S		0.5–2 2–10 5–10	1.4 1.4 1.4	346 251 110	$380 \pm 80$ $1300 \pm 100$ $940 \pm 100$		$1.63 \pm 0.13$ $1.61 \pm 0.10$ $1.35 \pm 0.15$		$\sim 13$ $\sim 8$	0.06 0.45 1	50 90 40	D D D	D D D	Rosati et al. (2002)
SESSI	2.1	2–10	1.5	478	$\sim 43.65^{+2.1}_{-2.0}$ $\sim 46.8 \pm 2.1$	10 10	$1.41 \pm 0.17$		$\sim 11$ $\sim 11$	1 1	100 100	D D	D D	H03
ELAIS	0.17	0.5–2 2–8 0.5–8	1.7 1.7 1.7	182 124 225	630 3548 1258		$1.72 \pm 0.09$ $2.07 \pm 0.15$ $1.70 \pm 0.08$			0.57 2.7 1.4	26 63 70	D D D	S S S	Manners et al. (2003)
BMW <sup>a</sup>	91.64	0.5–2	1.4	4786	$6150^{+1800}_{-1650}$		$1.82^{+0.07}_{-0.09}$	$0.60^{+0.02}_{-0.03}$	$14.8^{+1.27}_{-1.31}$	0.02	10000	D	N†	M03
ASCA <sup>b</sup>	73.71	2–10	1.4	1026	$5300^{+2850}_{-1400}$		$1.57^{+0.10}_{-0.08}$	$0.44^{+0.12}_{-0.13}$	$4.5^{+3.7}_{-1.7}$	0.21	8000	D	N†	
CDF-N+CDF-S	0.2	0.5–2 2–8	1.4 1.4	724 520	$3039^{+188}_{-108}$ $7403^{+125}_{-599}$		$0.55 \pm 0.03$ $0.56 \pm 0.14$			0.02 0.19	83.73 140.80	C C	S S	B04
ChaMP	1.1	0.5–2 2–8	1.7 1.4	707 236	$2030 \pm 210$ $3160 \pm 250$	1	$1.40 \pm 0.30$	$2.2 \pm 0.20$ $2.10 \pm 0.10$	$6 \pm 2$	0.6 4	100 400	D C	B S	KD04
CLASXS	0.4	0.5–2 0.5–2 2–8 2–8	1.4 1.4 1.4 1.4	310 310 235 235	$12.49 \pm 0.02$ 78.81 $38.1 \pm 0.2$ $45.60 \pm 0.5$		$1.7 \pm 0.2$  $1.65 \pm 0.4$	$2.5(fixed)$  $2.4 \pm 0.6$	$\sim 10$ $\sim 10$ $10 \sim 30$ $10 \sim 30$	0.5 0.5 3 3	35 35 90 90	D D D D	D D D D	Yang et al. (2004)
XMM/2dF	2	0.5–2 0.5–8		432 462			$1.8 \pm 0.2$		$\sim 60$ $\sim 60$	2.7 6.0 6.0	$\sim 500$ $\sim 700$ $\sim 700$	D D D	D D D	Basilakos et al. (2005)
XMM-LSS	3.4	0.5–2 0.5–2 2–10 2–10	1.7 1.7 1.7 1.7	1028 1028 328 328	384.2 6515  $4.5 \times 10^4$	1 1 1 1	$1.42^{+0.14}_{-0.15}$  $1.53^{+0.51}_{-1.16}$	$2.62^{+0.25}_{-0.22}$  $2.91^{+0.45}_{-0.30}$	$10.6^{+3.0}_{-2.2}$ $10.6^{+3.0}_{-2.2}$ $21.4^{+8.1}_{-3.4}$ $21.4^{+8.1}_{-5.4}$	$\sim 1$ $\sim 1$ $\sim 7$ $\sim 7$	700 700 500 500	D D D D	D D D D	Chiappetti et al. (2005)
ChaMP	9.6	0.5–2 2–8 0.5–8 0.3–2.5 2.5–8 0.3–8	1.4 1.4 1.4 1.4 1.4 1.4	4554 3078 5229 4864 2575 5515	$607^{+12}_{-12}$ $2040^{+50}_{-50}$ $1557^{+28}_{-50}$ $769^{+14}_{-14}$ $1828^{+48}_{-43}$ $1614^{+28}_{-43}$	1 1 1 1 1 1	$1.54^{+0.02}_{-0.02}$ $1.82^{+0.01}_{-0.01}$ $1.64^{+0.01}_{-0.01}$ $1.57^{+0.01}_{-0.01}$ $1.81^{+0.01}_{-0.01}$ $1.65^{+0.01}_{-0.01}$	$2.36^{+0.05}_{-0.05}$ $2.65^{+0.07}_{-0.07}$ $2.48^{+0.05}_{-0.05}$ $2.41^{+0.05}_{-0.05}$ $2.58^{+0.05}_{-0.05}$ $2.44^{+0.06}_{-0.05}$	$6.8^{+0.5}_{-0.5}$ $19.2^{+6.3}_{-1.8}$ $22.9^{+1.6}_{-1.6}$ $9.9^{+0.7}_{-0.6}$ $14.2^{+0.9}_{-1.1}$ $25.0^{+1.9}_{-1.4}$	0.26 1.17 0.69 0.33 1.27 0.63	2395.21 7112.31 6767.74 3286.49 6690.72 7175.62	D D D D D D	B B B B B B	this study
ChaMP + CDFs	9.8	0.5–2 2–8	1.4 1.4	4554 + 724 3078 + 520	$571^{+11}_{-11}$ $1258^{+29}_{-29}$	1 1	$1.49^{+0.02}_{-0.01}$ $1.58^{+0.01}_{-0.01}$	$2.36^{+0.05}_{-0.05}$ $2.59^{+0.06}_{-0.05}$	$6.5^{+0.4}_{-0.4}$ $14.4^{+0.9}_{-0.9}$	0.02 0.19	2395.21 7112.31	D D	B B	this study

Note. — Col. (1): used data. <sup>a</sup>BMW (Brera Multiscale Wavelet)-HRI, HELLAS2XMM, BMW-CDFS, and BMW-HDF. <sup>b</sup>ASCA-HSS, HELLAS2XMM, BMW-CDFS, and BMW-HDF. Col. (2): sky coverage of the sample in units of  $deg^2$ . Col. (3): X-ray energy band in units of keV. Col. (4): assumed photon index. Col. (5): source numbers in the sample. Col. (6): normalization constant. Col. (7): normalization flux in units of  $10^{-15} erg cm^{-2} sec^{-1}$ . Col. (8): faint power law index. Col. (9): bright power law index. Col. (10): break flux in units of  $10^{-15} erg cm^{-2} sec^{-1}$ . Col. (11): faint flux limit of the sample in units of  $10^{-15} erg cm^{-2} sec^{-1}$ . Col. (12): bright flux limit of the sample in units of  $10^{-15} erg cm^{-2} sec^{-1}$ . Col. (13): fitting domain. C: cumulative number count, D: differential number count. Col. (14): fitting formula. S: single power law, B: broken power law, D: double power law, N: nonlinear formula, see equation (5) in text. Col. (15): reference.

Table 5. List of the Best Fit Parameters of the Soft and Hard Sources

$\Gamma_{ph}$	Band	Soft Source (HR < 0)					Hard Source (HR > 0)		
		N	K	$\gamma_1$	$\gamma_2$	$S_b$	N	K	$\gamma$
(1)	(2)	(3)	(4)	(5)	(6)	(7)	(8)	(9)	(10)
1.4	S	4289	$580^{+12}_{-12}$	$1.43^{+0.02}_{-0.02}$	$2.35^{+0.04}_{-0.04}$	$8.5^{+0.5}_{-0.5}$	575	$217^{+22}_{-20}$	$2.45^{+0.08}_{-0.07}$
	H	1787	$896^{+31}_{-31}$	$1.63^{+0.02}_{-0.02}$	$2.58^{+0.08}_{-0.07}$	$13.5^{+1.1}_{-1.3}$	787	$1614^{+209}_{-184}$	$2.35^{+0.05}_{-0.05}$
	B	4427	$900^{+18}_{-31}$	$1.46^{+0.01}_{-0.01}$	$2.35^{+0.04}_{-0.04}$	$20.6^{+1.4}_{-1.3}$	1088	$1195^{+106}_{-98}$	$2.34^{+0.04}_{-0.04}$
1.7	S	4289	$588^{+12}_{-12}$	$1.44^{+0.02}_{-0.02}$	$2.34^{+0.04}_{-0.04}$	$8.7^{+0.6}_{-0.5}$	575	$237^{+23}_{-22}$	$2.46^{+0.08}_{-0.07}$
	H	1787	$898^{+31}_{-31}$	$1.64^{+0.02}_{-0.02}$	$2.59^{+0.07}_{-0.07}$	$13.1^{+0.9}_{-1.3}$	787	$1508^{+192}_{-170}$	$2.35^{+0.05}_{-0.05}$
	B	4427	$924^{+17}_{-31}$	$1.51^{+0.01}_{-0.02}$	$2.42^{+0.06}_{-0.09}$	$21.0^{+1.5}_{-4.0}$	1088	$1037^{+86}_{-80}$	$2.35^{+0.04}_{-0.04}$
1.4	Sc	4149	$521^{+11}_{-11}$	$1.47^{+0.02}_{-0.02}$	$2.35^{+0.05}_{-0.05}$	$6.7^{+0.5}_{-0.4}$	405	$101^{+11}_{-10}$	$2.47^{+0.10}_{-0.10}$
	Hc	2185	$1129^{+33}_{-33}$	$1.69^{+0.01}_{-0.01}$	$2.57^{+0.07}_{-0.07}$	$16.4^{+4.4}_{-1.5}$	893	$1509^{+182}_{-163}$	$2.30^{+0.05}_{-0.04}$
	Bc	4235	$916^{+18}_{-33}$	$1.49^{+0.01}_{-0.01}$	$2.45^{+0.05}_{-0.05}$	$21.8^{+1.4}_{-1.4}$	994	$1160^{+116}_{-105}$	$2.37^{+0.05}_{-0.04}$
1.7	Sc	4149	$525^{+11}_{-11}$	$1.47^{+0.02}_{-0.02}$	$2.35^{+0.05}_{-0.05}$	$6.8^{+0.5}_{-0.5}$	405	$100^{+10}_{-10}$	$2.44^{+0.10}_{-0.09}$
	Hc	2185	$1060^{+31}_{-31}$	$1.68^{+0.01}_{-0.01}$	$2.58^{+0.07}_{-0.07}$	$15.4^{+2.0}_{-1.4}$	893	$1378^{+164}_{-147}$	$2.30^{+0.05}_{-0.05}$
	Bc	4235	$842^{+17}_{-31}$	$1.48^{+0.01}_{-0.01}$	$2.44^{+0.05}_{-0.05}$	$18.1^{+1.2}_{-3.0}$	994	$946^{+87}_{-81}$	$2.38^{+0.05}_{-0.04}$

Note. — Col. (1): assumed photon index. Col. (2): X-ray energy band (see Table 1). Col. (3): number of sources with a hardness ratio of HR < 0. Col. (4): normalization constant of a broken power law. Col. (5): faint power law index of a broken power law. Col. (6): bright power law index of a broken power law. Col. (7): break flux in units of  $10^{-15} \text{ erg cm}^{-2} \text{ sec}^{-1}$ . Col. (8): number of sources with a hardness ratio of HR > 0. Col. (9): normalization constant of a single power law. Col. (10): power law index of a single power law.

Table 6. Break Factor

$\Gamma_{ph}$	Band	Total	HR < 0
(1)	(2)	(3)	(4)
1.4	B	0.19	0.23
	S	0.21	0.24
	H	0.18	0.23
	Bc	0.20	0.24
	Sc	0.21	0.23
	Hc	0.18	0.21
1.7	B	0.20	0.21
	S	0.21	0.24
	H	0.18	0.22
	Bc	0.20	0.25
	Sc	0.21	0.23
	Hc	0.18	0.21

Note. — Col. (1): assumed photon index. Col. (2): X-ray energy band (see Table 1). Col. (3): break factor for the total sample. Col. (4): break factor for the soft sample (HR < 0).

Table 7. List of the Best Fit Parameters including Target Objects

DATA	$\Gamma_{ph}$	Band	$K$	$\gamma_1$	$\gamma_2$	$S_b$
(1)	(2)	(3)	(4)	(5)	(6)	(7)
ChaMP	1.4	S	$753^{+15}_{-15}$	$1.54^{+0.02}_{-0.01}$	$2.31^{+0.04}_{-0.04}$	$8.6^{+0.7}_{-0.6}$
		H	$1856^{+53}_{-48}$	$1.81^{+0.01}_{-0.01}$	$2.48^{+0.05}_{-0.06}$	$14.0^{+0.9}_{-1.6}$
		B	$1550^{+28}_{-48}$	$1.62^{+0.01}_{-0.01}$	$2.31^{+0.04}_{-0.04}$	$21.0^{+4.7}_{-1.6}$
	1.7	S	$766^{+15}_{-15}$	$1.55^{+0.01}_{-0.01}$	$2.31^{+0.04}_{-0.04}$	$9.0^{+1.7}_{-0.6}$
		H	$1825^{+50}_{-41}$	$1.82^{+0.01}_{-0.01}$	$2.48^{+0.04}_{-0.05}$	$13.5^{+0.7}_{-1.4}$
		B	$1469^{+26}_{-41}$	$1.63^{+0.01}_{-0.01}$	$2.34^{+0.04}_{-0.04}$	$19.3^{+3.6}_{-1.4}$
	1.4	Sc	$610^{+12}_{-12}$	$1.54^{+0.02}_{-0.02}$	$2.30^{+0.05}_{-0.04}$	$6.6^{+0.5}_{-0.5}$
		Hc	$2038^{+50}_{-50}$	$1.82^{+0.01}_{-0.01}$	$2.54^{+0.07}_{-0.06}$	$18.5^{+2.5}_{-2.1}$
		Bc	$1561^{+27}_{-50}$	$1.64^{+0.01}_{-0.01}$	$2.40^{+0.05}_{-0.05}$	$22.1^{+1.7}_{-1.7}$
ChaMP+ CDFs	1.4	Sc	$574^{+12}_{-12}$	$1.49^{+0.02}_{-0.02}$	$2.29^{+0.05}_{-0.10}$	$6.2^{+0.5}_{-1.4}$
		Hc	$1240^{+55}_{-55}$	$1.55^{+0.02}_{-0.02}$	$2.44^{+0.04}_{-0.04}$	$11.9^{+0.8}_{-0.7}$
	1.7	Sc	$615^{+12}_{-12}$	$1.53^{+0.02}_{-0.02}$	$2.29^{+0.04}_{-0.04}$	$6.5^{+0.5}_{-0.5}$
		Hc	$1930^{+47}_{-47}$	$1.82^{+0.01}_{-0.01}$	$2.53^{+0.07}_{-0.07}$	$17.1^{+2.0}_{-2.2}$
		Bc	$1410^{+25}_{-47}$	$1.64^{+0.01}_{-0.01}$	$2.39^{+0.05}_{-0.05}$	$18.4^{+1.5}_{-1.4}$
	1.4	Sc	$574^{+12}_{-12}$	$1.49^{+0.02}_{-0.02}$	$2.29^{+0.05}_{-0.10}$	$6.2^{+0.5}_{-1.4}$
		Hc	$1240^{+55}_{-55}$	$1.55^{+0.02}_{-0.02}$	$2.44^{+0.04}_{-0.04}$	$11.9^{+0.8}_{-0.7}$

Note. — Col. (1): used data set. Col. (2): assumed photon index. Col. (3): X-ray energy band (see Table 1). Col. (4): normalization constant. Col. (5): faint power law index of a broken power law. Col. (6): bright power law index of a broken power law. Col. (7): break flux in units of  $10^{-15} \text{ erg cm}^{-2} \text{ sec}^{-1}$ .

Table 8. The Resolved Cosmic X-ray Background Flux Density

Data (1)	Band (2)	$f_{min}$ (3)	$f_{max}$ (4)	$CXRB_{total}$ (5)	$CXRB_{nt}$ (6)	$Fraction_{nt}[\%]$ (7)	$CXRB_{yt}$ (8)	$Fraction_{yt}[\%]$ (9)
ChaMP	B	0.63	0.72	$2.70 \pm 0.12$	$2.10^{+0.04}_{-0.04}$	$77.6^{+1.3}_{-1.3}$	$2.29^{+0.04}_{-0.04}$	$84.9^{+1.5}_{-1.5}$
	S	0.33	0.33	$1.10 \pm 0.05$	$0.82^{+0.02}_{-0.02}$	$74.7^{+1.4}_{-1.4}$	$0.89^{+0.02}_{-0.02}$	$81.5^{+1.6}_{-1.6}$
	H	1.27	0.67	$1.59 \pm 0.10$	$1.10^{+0.03}_{-0.03}$	$69.4^{+1.8}_{-1.6}$	$1.19^{+0.03}_{-0.03}$	$74.5^{+2.1}_{-1.9}$
	Bc	0.69	0.68	$2.54 \pm 0.12$	$1.88^{+0.03}_{-0.03}$	$74.0^{+1.3}_{-1.3}$	$2.01^{+0.04}_{-0.04}$	$79.2^{+1.4}_{-1.4}$
	Sc	0.26	0.24	$0.75 \pm 0.04$	$0.60^{+0.01}_{-0.01}$	$80.1^{+1.6}_{-1.6}$	$0.65^{+0.01}_{-0.01}$	$86.3^{+1.7}_{-1.7}$
	Hc	1.17	0.71	$1.79 \pm 0.11$	$1.28^{+0.03}_{-0.03}$	$71.6^{+1.7}_{-1.7}$	$1.36^{+0.03}_{-0.03}$	$76.1^{+1.8}_{-1.8}$
ChaMP+	Sc	0.02	0.24	$0.75 \pm 0.04$	$0.63^{+0.01}_{-0.01}$	$84.4^{+1.6}_{-1.6}$	$0.68^{+0.01}_{-0.01}$	$90.7^{+1.9}_{-1.9}$
CDFs	Hc	0.20	0.71	$1.79 \pm 0.11$	$1.40^{+0.03}_{-0.03}$	$78.1^{+1.8}_{-1.8}$	$1.50^{+0.07}_{-0.07}$	$84.0^{+3.7}_{-3.7}$

Note. — Col. (1): used data set. Col. (2): X-ray energy band (see Table 1). Col. (3)-(4): faint and bright flux limits of the data in units of  $10^{-15} \text{ erg cm}^{-2} \text{ sec}^{-1}$  and  $10^{-11} \text{ erg cm}^{-2} \text{ sec}^{-1}$ , respectively. Col. (5): total CXRB flux density in units of  $10^{-11} \text{ erg cm}^{-2} \text{ sec}^{-1} \text{ deg}^{-2}$ . The total CXRB flux densities in the Sc and Hc bands are from B04. The total CXRB flux density in the Bc band is the sum of those in the Sc and Hc bands. The total CXRB flux densities in the B, S, and H bands are rescaled from those in the Bc, Sc, and Hc bands by assuming  $\Gamma_{ph} = 1.1$ . Col. (6): the resolved CXRB flux density without target sources in units of  $10^{-11} \text{ erg cm}^{-2} \text{ sec}^{-1} \text{ deg}^{-2}$ . Col. (7): the percentage of the resolved CXRB excluding target sources. Col. (8): the resolved CXRB flux density with target sources in units of  $10^{-11} \text{ erg cm}^{-2} \text{ sec}^{-1} \text{ deg}^{-2}$ . Col. (9): the percentage of the resolved CXRB including target sources.



Table 9. The Total Cosmic X-ray Background Flux Density

Band	Unresolved CXRB	Unresolved CXRB [%]	Resolved CXRB	Resolved CXRB [%]	Total CXRB	Reference
(1)	(2)	(3)	(4)	(5)	(6)	(7)
0.5-2	—	—	—	$94.3^{+7.0}_{-6.7}$	$0.75^{+0.04}_{-0.04}$	M03
2-10	—	—	—	$88.8^{+7.8}_{-6.6}$	$2.02^{+0.11}_{-0.11}$	
0.5-2	—	—	—	$89.5^{+5.9}_{-5.7}$	$0.75^{+0.04}_{-0.04}$	B04
2-8	—	—	—	$92.6^{+6.6}_{-6.3}$	$1.79^{+0.11}_{-0.11}$	
1-2	$0.10^{+0.01}_{-0.01}$	$22.7^{+3.1}_{-3.1}$	$0.35^{+0.02}_{-0.02}$	$77.0^{+3.0}_{-3.0}$	$0.46^{+0.03}_{-0.03}$	HM06
2-8	$0.34^{+0.17}_{-0.17}$	$20.0^{+10.0}_{-10.0}$	$1.36^{+0.10}_{-0.10}$	$80.0^{+8.0}_{-8.0}$	$1.70^{+0.20}_{-0.20}$	
0.5-2	$0.18^{+0.03}_{-0.03}$	$21.9^{+3.8}_{-3.8}$	$0.63^{+0.01}_{-0.01}$	$78.1^{+1.2}_{-1.2}$	$0.81^{+0.03}_{-0.03}$	this study
1-2	$0.10^{+0.01}_{-0.01}$	$21.5^{+2.9}_{-2.9}$	$0.38^{+0.01}_{-0.01}$	$78.5^{+1.2}_{-1.2}$	$0.48^{+0.02}_{-0.02}$	without targets
2-8	$0.34^{+0.17}_{-0.17}$	$19.5^{+9.8}_{-9.8}$	$1.40^{+0.03}_{-0.03}$	$80.5^{+1.7}_{-1.7}$	$1.74^{+0.17}_{-0.17}$	
0.5-2	$0.18^{+0.03}_{-0.03}$	$20.7^{+3.6}_{-3.6}$	$0.68^{+0.01}_{-0.01}$	$79.3^{+1.2}_{-1.2}$	$0.86^{+0.03}_{-0.03}$	this study
1-2	$0.10^{+0.01}_{-0.01}$	$20.2^{+2.7}_{-2.7}$	$0.41^{+0.01}_{-0.01}$	$79.8^{+1.2}_{-1.2}$	$0.51^{+0.02}_{-0.02}$	with targets
2-8	$0.34^{+0.17}_{-0.17}$	$18.5^{+9.2}_{-9.2}$	$1.50^{+0.07}_{-0.07}$	$81.5^{+3.8}_{-3.8}$	$1.84^{+0.18}_{-0.18}$	

Note. — Col. (1): X-ray energy band in keV. Col. (2): the unresolved CXRB flux density (HM05) in units of  $10^{-11} \text{ erg cm}^{-2} \text{ sec}^{-1} \text{ deg}^{-2}$ . Col. (3): the percentage of the total CXRB flux density that is unresolved. Col. (4): the resolved CXRB flux density from the ChaMP+CDFs number counts in units of  $10^{-11} \text{ erg cm}^{-2} \text{ sec}^{-1} \text{ deg}^{-2}$ . The resolved CXRB in the 1-2 keV band is rescaled from that in the 0.5-2 keV band assuming  $\Gamma_{ph} = 1.4$ . Col. (5): the percentage of the total CXRB flux density that is resolved. Col. (6): the total CXRB flux density in units of  $10^{-11} \text{ erg cm}^{-2} \text{ sec}^{-1} \text{ deg}^{-2}$ . This column is the sum of the column (2) and the column (4) for HM05 and this study. Col. (7): reference

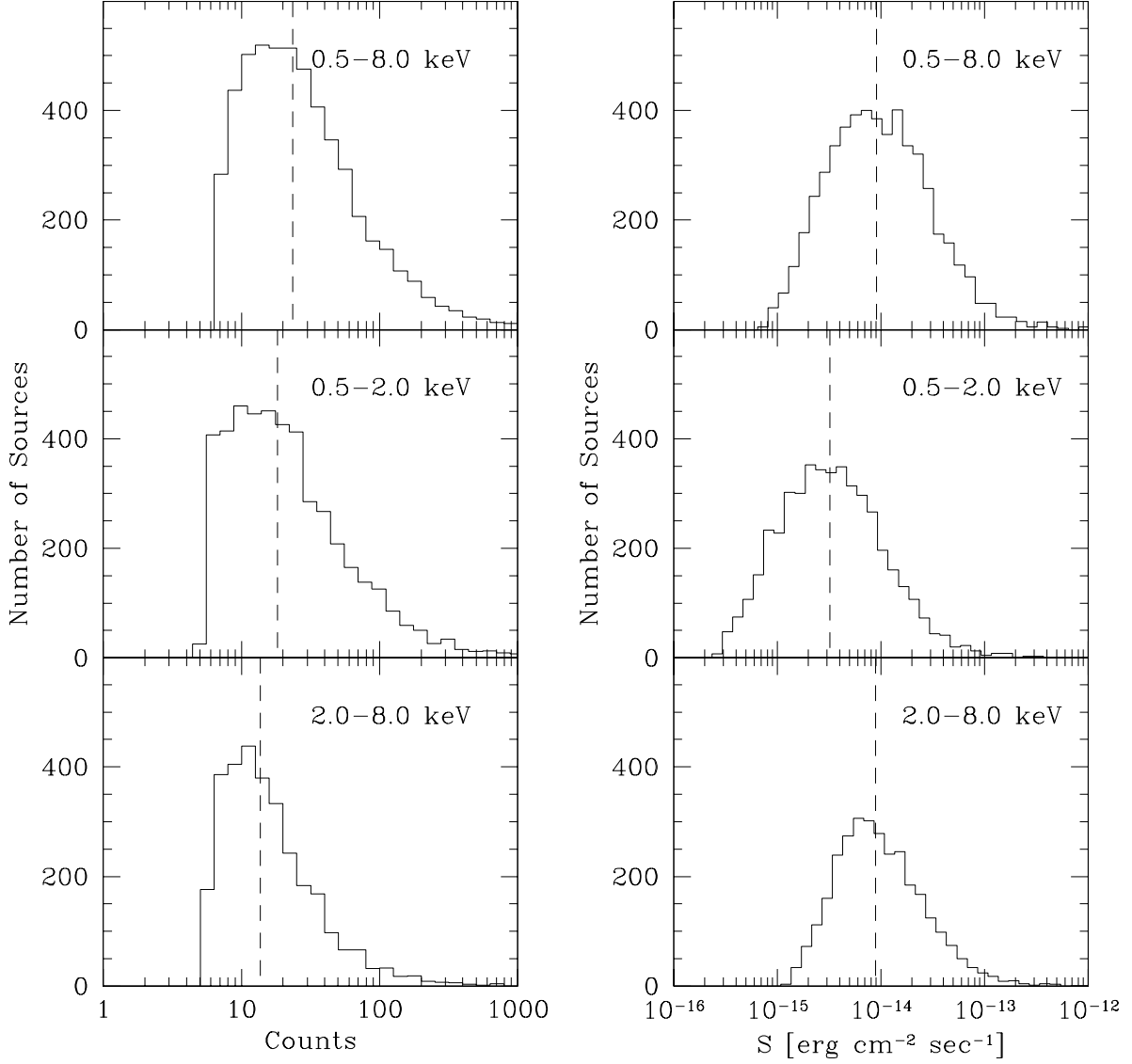


Fig. 1.— The distributions of source net counts (*left*) and flux (*right*) in three energy bands. The vertical dashed line indicates the median of the distribution. The flux was determined assuming a photon index of  $\Gamma_{ph} = 1.4$ .

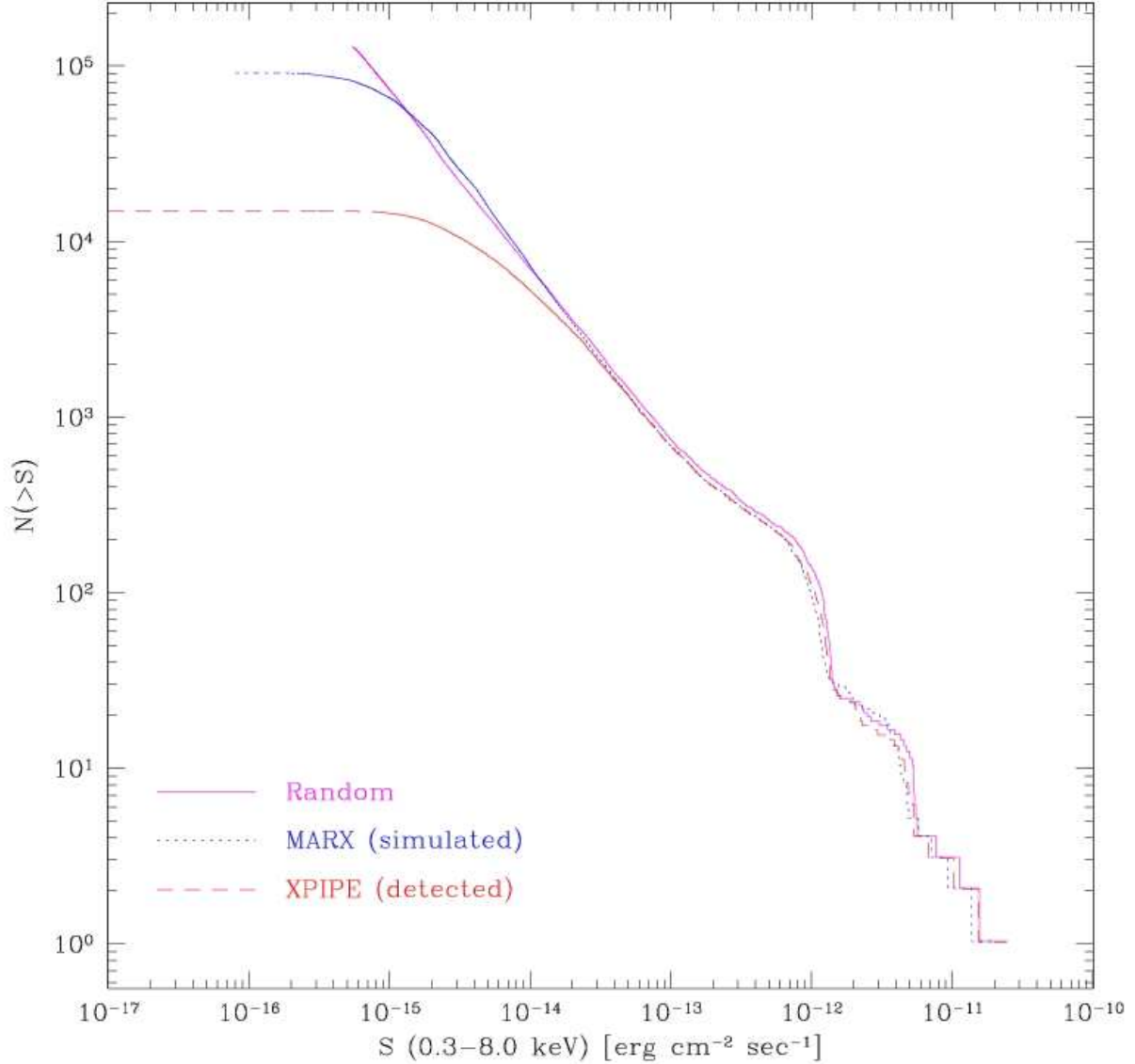


Fig. 2.— The cumulative number counts for the artificial sources in the B band. The magenta solid line represents the number counts for sources whose fluxes were randomly selected from the assumed number counts with a slope of  $-1$ . Due to small number statistics, deviations from the assumed number counts are present in the bright flux regime. Blue dotted and red dashed lines represent number counts for sources generated with MARX and for sources extracted with XPIPE, respectively. The effect of Eddington bias is evident at the faint fluxes ( $S < 10^{-14} \text{ erg cm}^{-2} \text{ sec}^{-1}$ ) in the simulated source number counts.

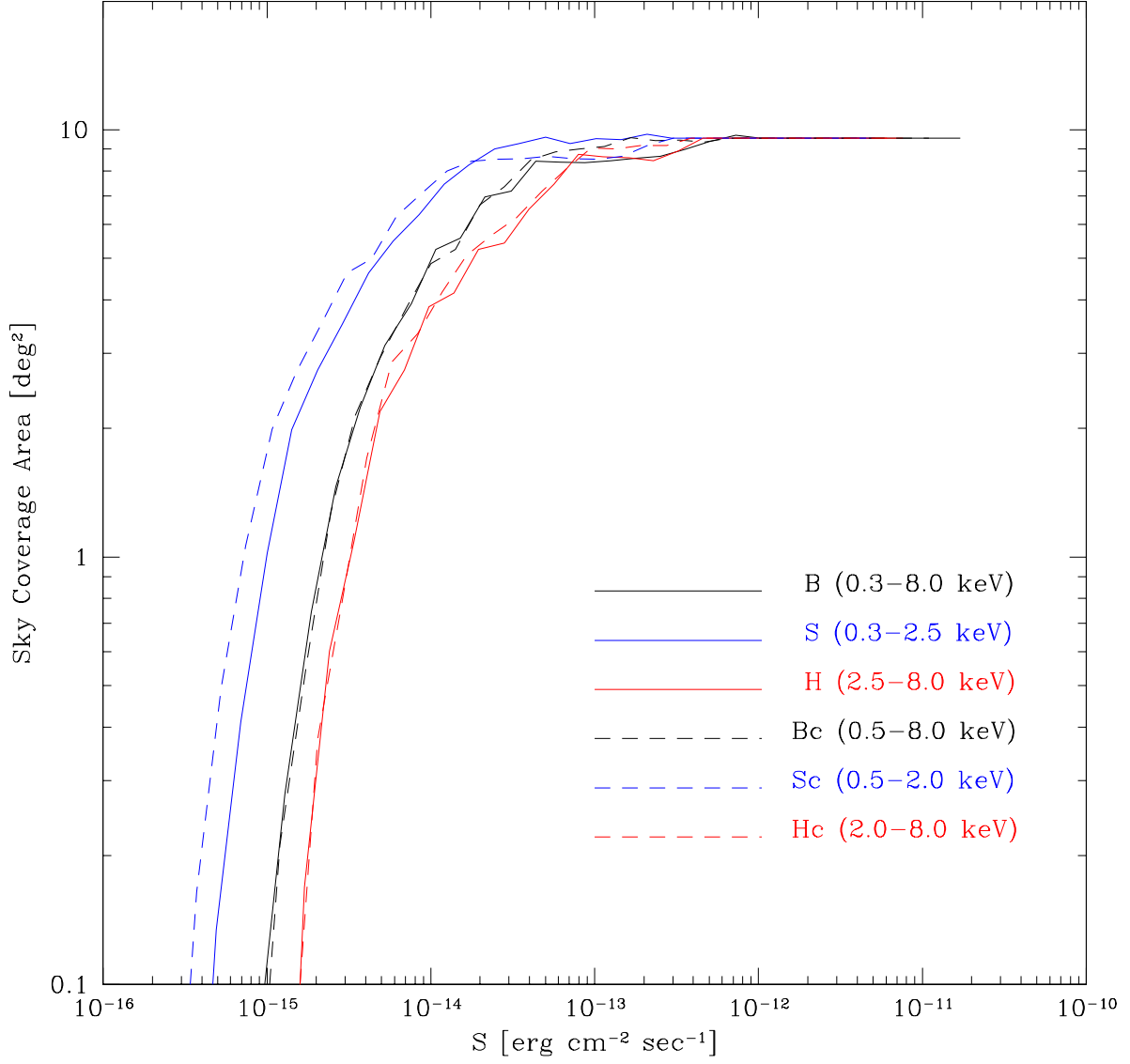


Fig. 3.— Sky coverages for sources with  $S/N > 1.5$  in six energy bands. The full sky coverage is  $9.6 \text{ deg}^2$ .

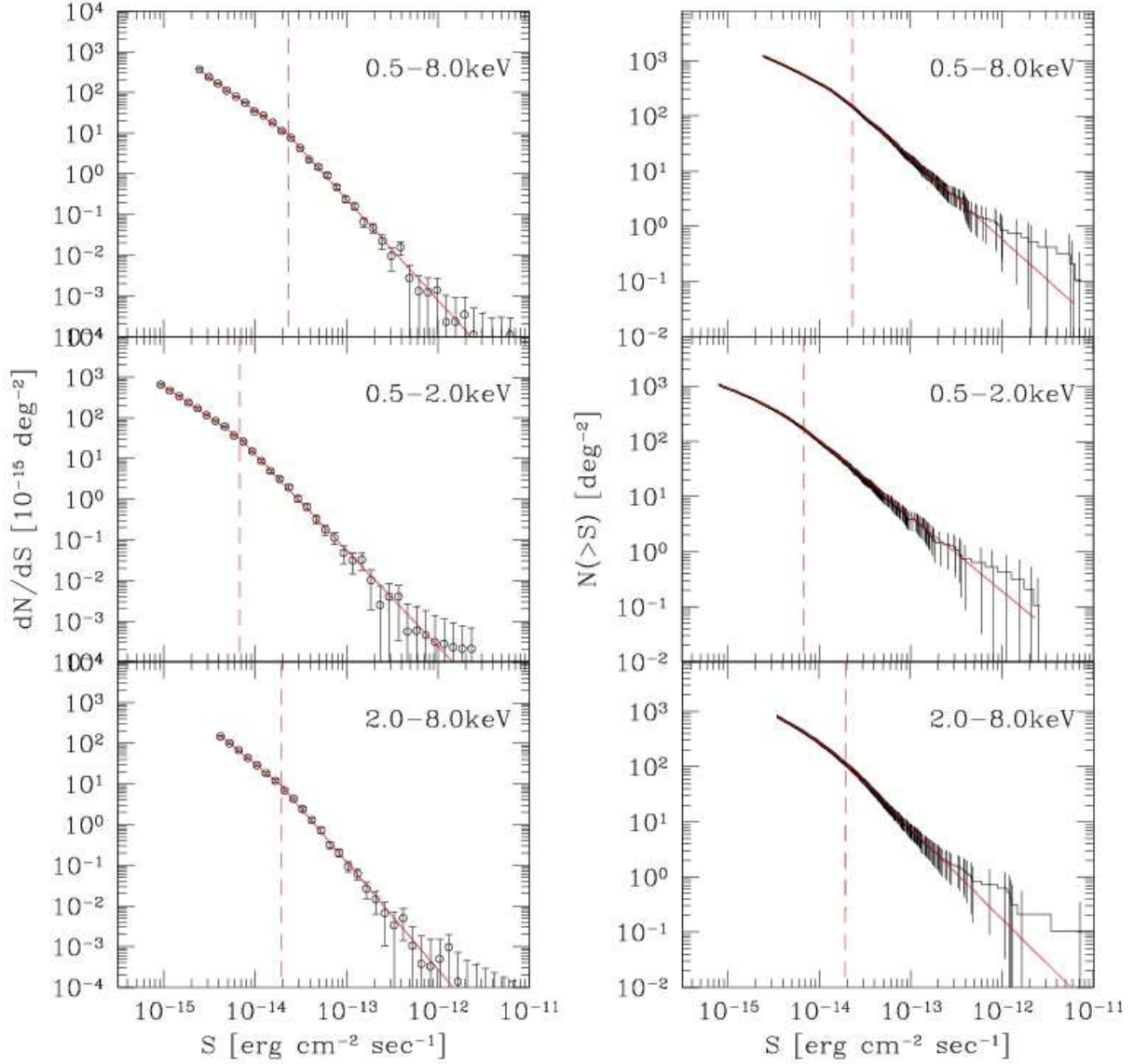


Fig. 4.— The differential (*left*) and cumulative (*right*) number counts of the ChaMP X-ray point sources in the Bc, Sc, and Hc bands, respectively. Red solid lines represent the best fit results with a broken power law. The vertical red dashed lines indicate the derived break fluxes. Source fluxes were determined assuming a photon index of  $\Gamma_{ph} = 1.4$ . Since we present the differential number counts brighter than a flux corresponding to 10% of the full sky coverage, the faintest bin still has sufficient sources and shows a small error bar. The error bars in the cumulative number counts are estimated by the error propagation rule using Gehrels et al. (1986) statistics.

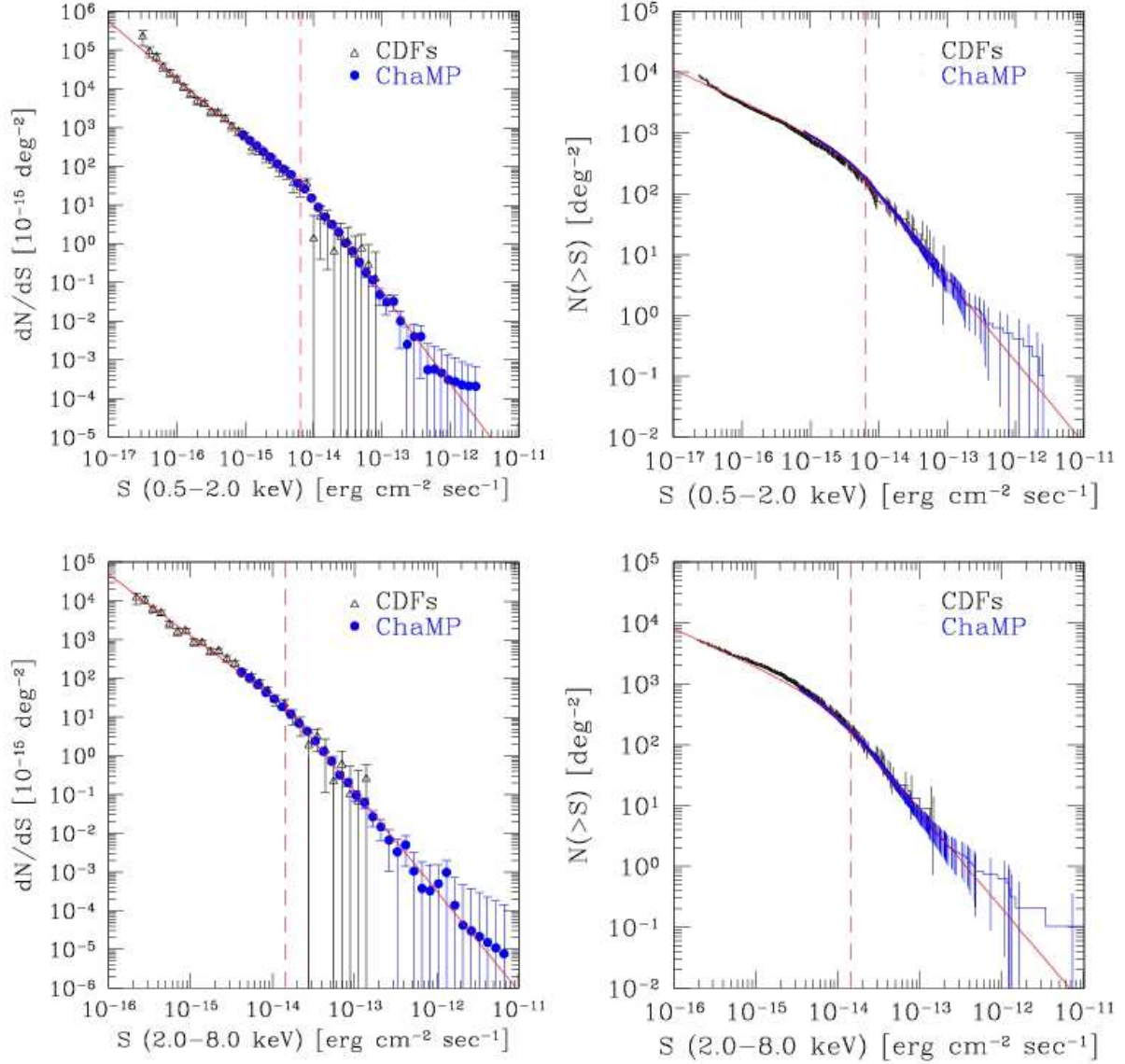


Fig. 5.— The differential (*left*) and cumulative (*right*) number counts for the ChaMP+CDFs X-ray point sources in the Sc and Hc bands. Blue filled circles and black open triangles represent the ChaMP and the CDFs data, respectively. Red lines are the best simultaneous fit results. The vertical dashed lines indicate the derived break fluxes. Source fluxes were determined assuming a photon index of  $\Gamma_{ph} = 1.4$ .

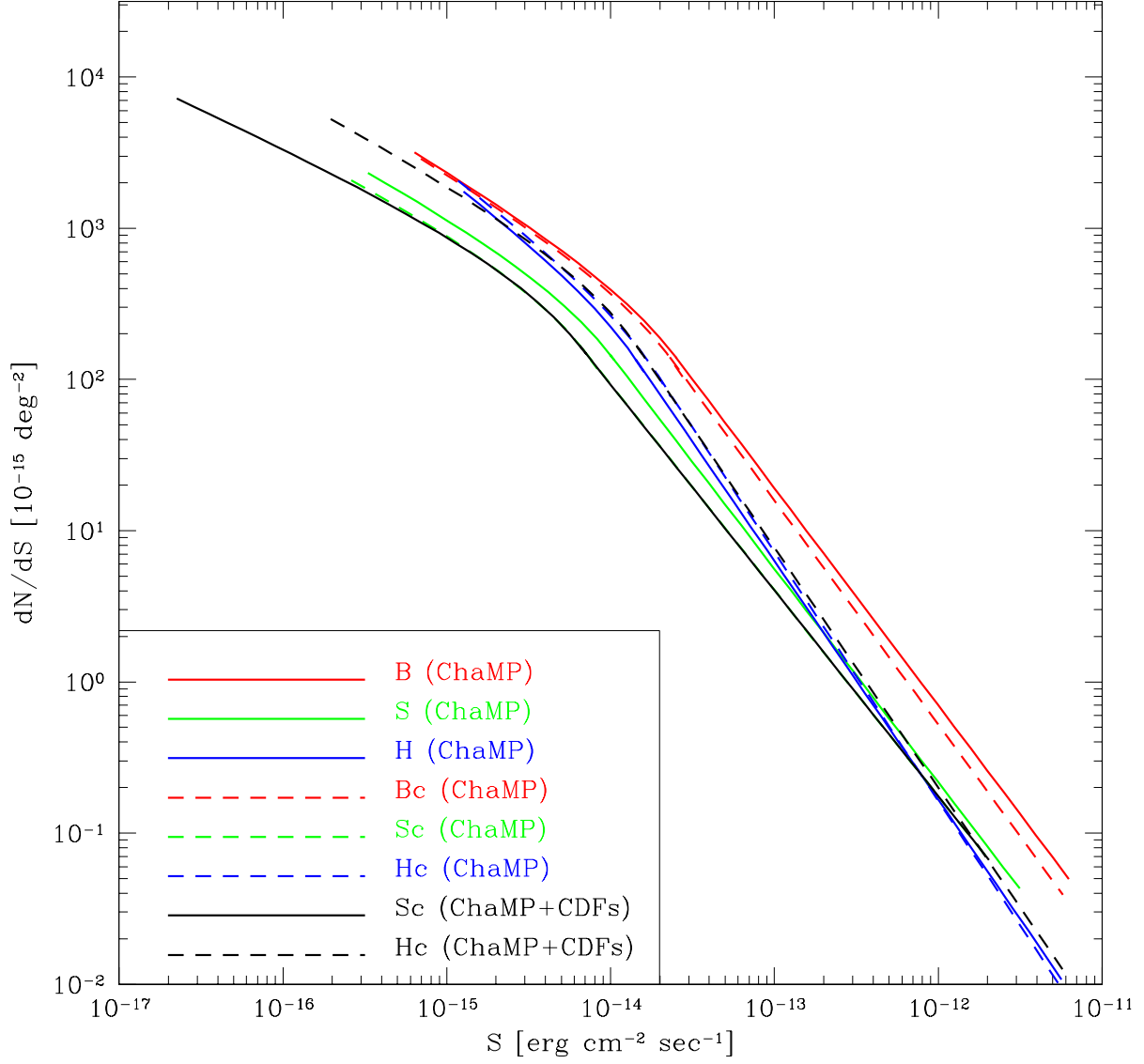


Fig. 6.— The differential number counts of the ChaMP and the ChaMP+CDFs from the best fit results in 6 energy bands. Source fluxes were determined assuming a photon index of  $\Gamma_{ph} = 1.4$ . For energy band definition, see Table 1.

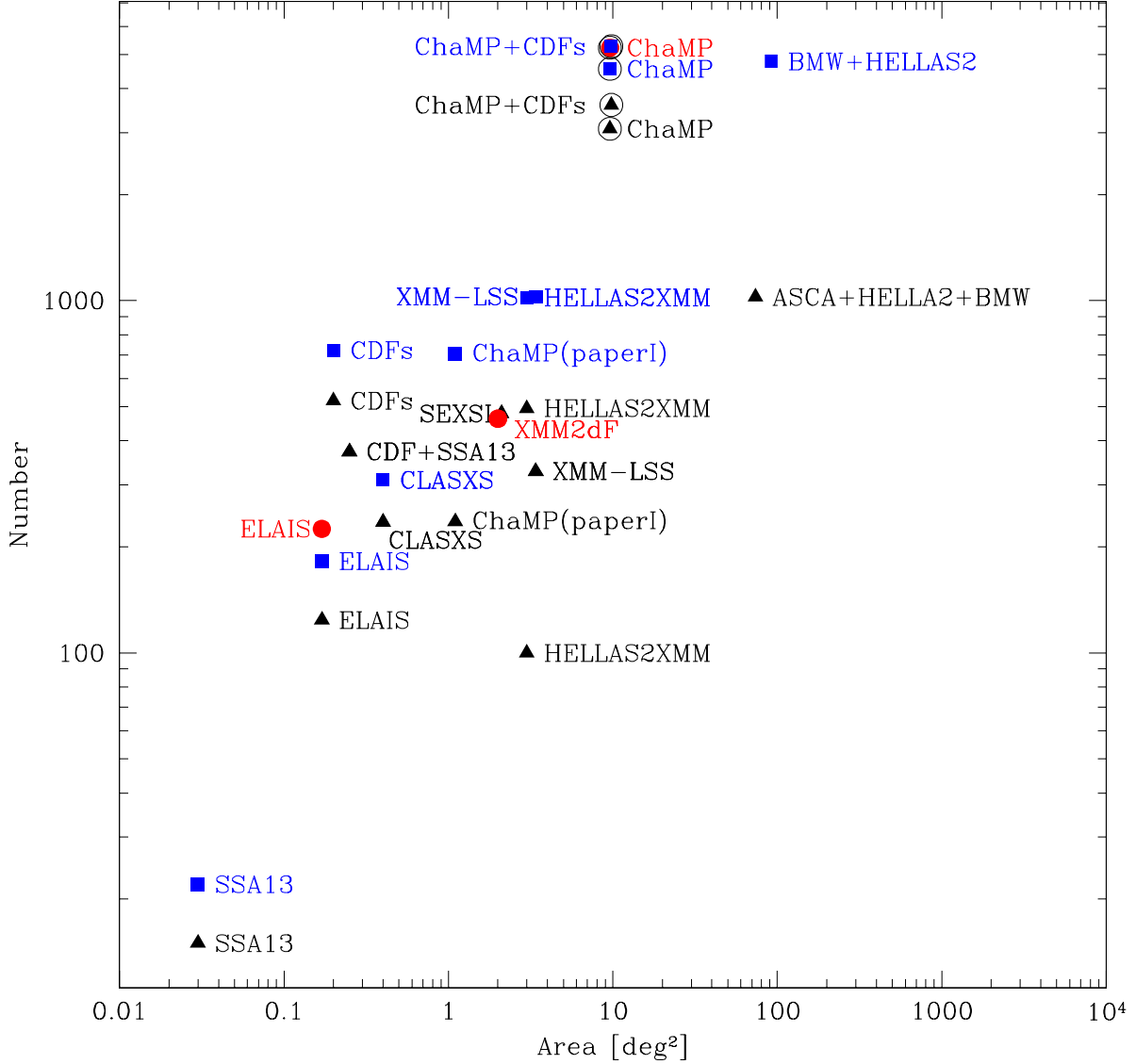


Fig. 7.— The number of sources and covered sky areas for various studies. Red circles, blue squares, and black triangles represent the broad, soft, and hard energy bands, respectively. References and parameters are listed in Table 4. The ChaMP contains  $\sim 5,200$  sources in the 0.5-8 keV band and covers  $9.6 \text{ deg}^2$  in sky area, and the ChaMP+CDFs covers  $9.8 \text{ deg}^2$ . For this study, the 0.5-2 keV, 2-8 keV, and 0.5-8 keV bands are used and are marked by open circles for clear comparison.



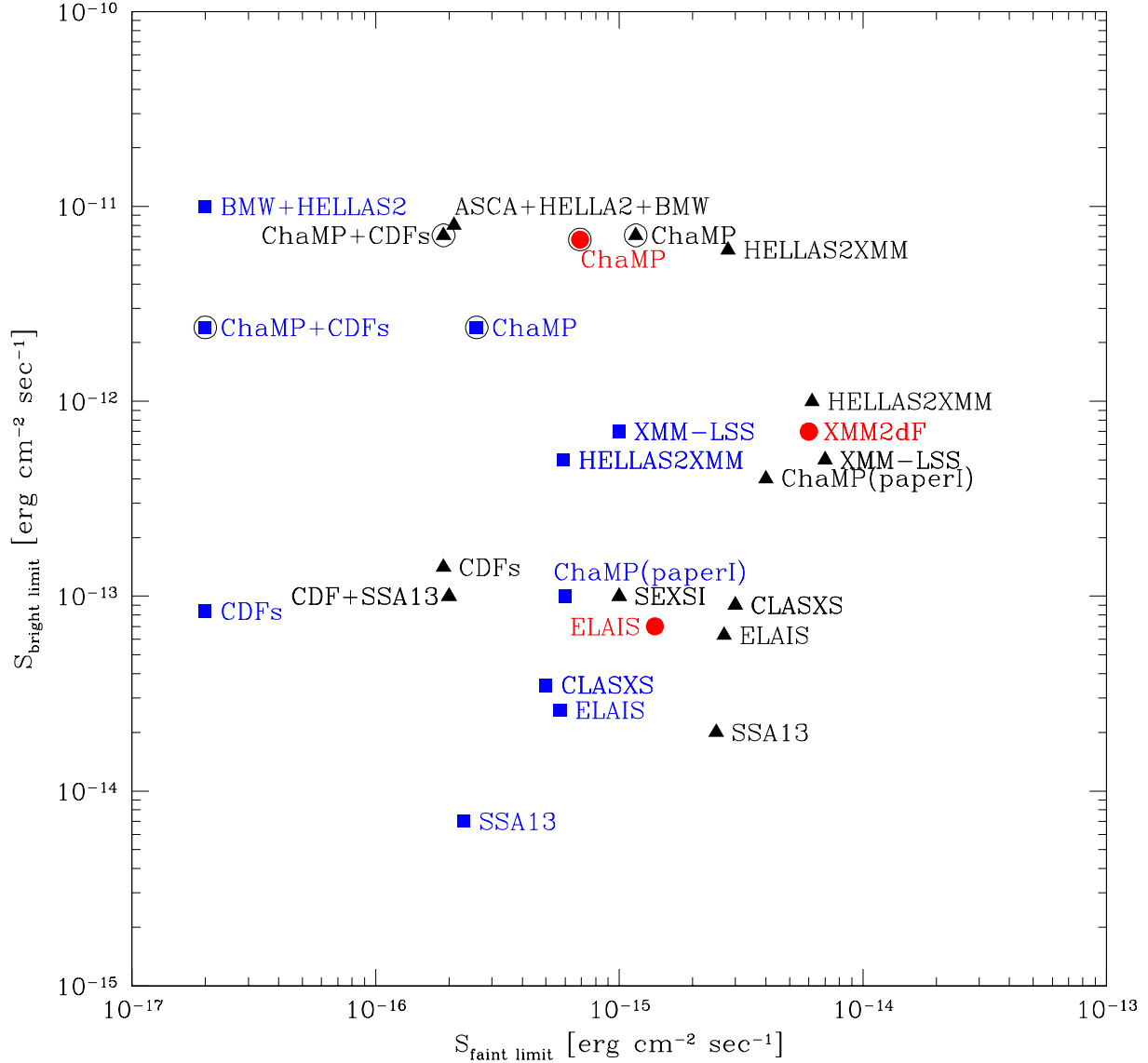


Fig. 8.— The faint and bright flux limits of various studies. Red circles, blue squares, and black triangles represent the broad, soft, and hard energy bands. References and parameters are listed in Table 4. For this study, the 0.5-2 keV, 2-8 keV, and 0.5-8 keV bands are used and are marked by open circles for clear comparison. We note that the faint and bright flux limit of the ChaMP are estimated from ChaMP sources with  $S/N > 1.5$ . For the other studies, the faint and bright flux limits are from the literature or from our own visual estimations based on their number counts.

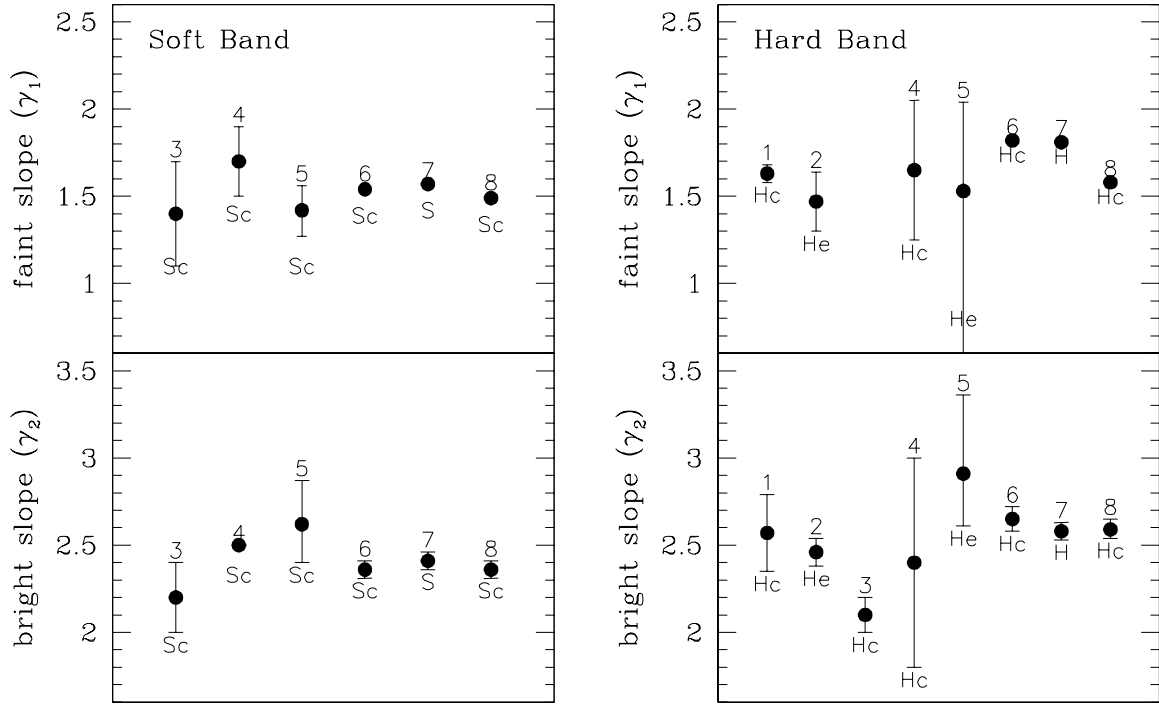


Fig. 9.— The faint (*top*) and bright (*bottom*) power indices of the differential number counts for this and previous studies in the soft (*left*) and the hard (*right*) bands, respectively. The references are marked by number: 1: Cowie et al. (2002), 2: H03, 3: KD04, 4: Yang et al. (2004), 5: Chiappetti et al. (2005), 6-7: This study for the ChaMP, and 8: This study for the ChaMP+CDF. The energy bands of each study are also marked here and for the definition of them, see Table 1. Note that Yang et al. (2004) fixed the bright slope as 2.5 in the Sc band having no error.

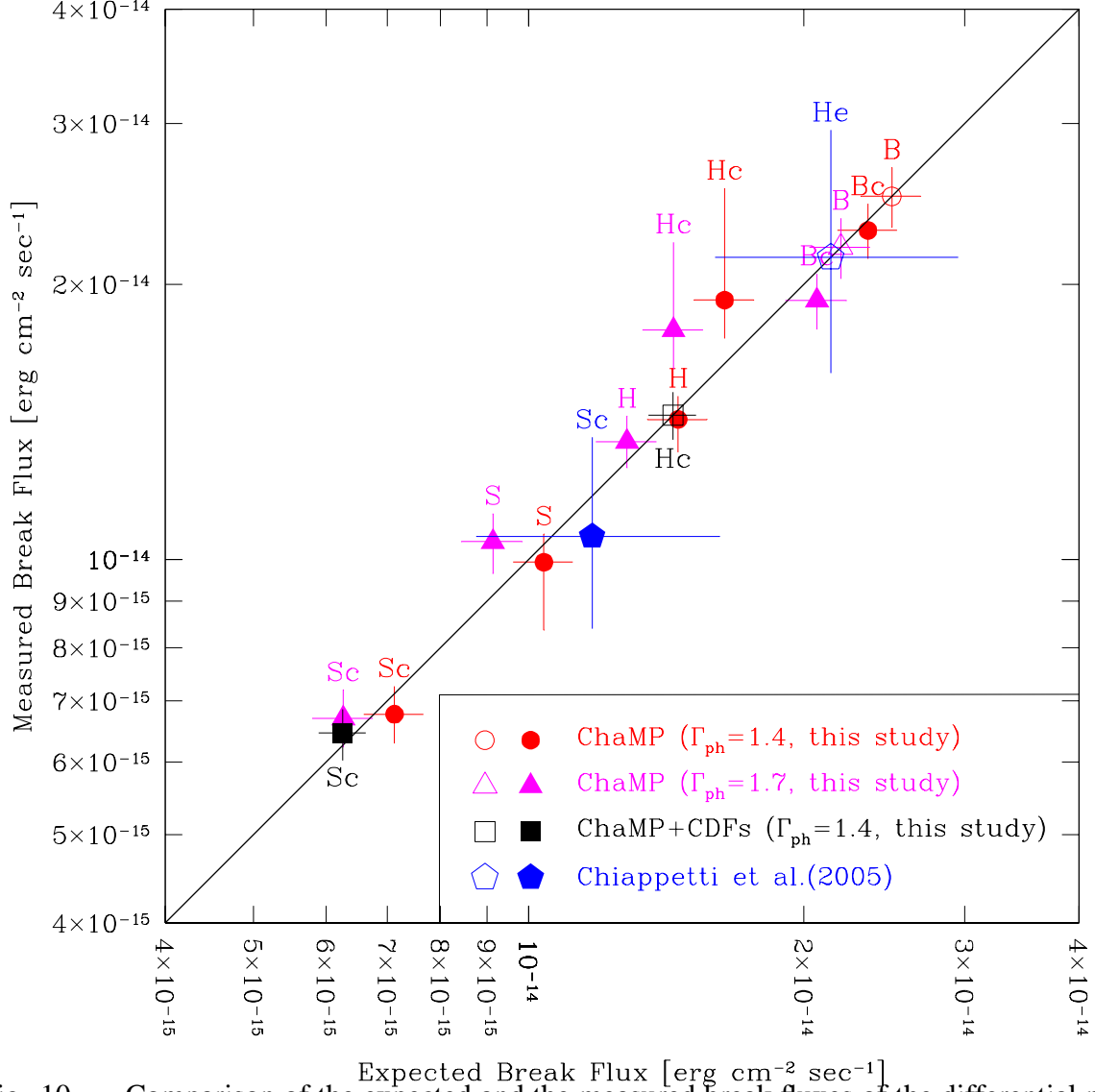


Fig. 10.— Comparison of the expected and the measured break fluxes of the differential number counts in various energy bands. Assuming a single power law model for the X-ray spectrum, the expected break flux in each band (*closed symbol*) was calculated by converting the  $S_b, std$  (see equation (7)) which is the measured break flux in the B (ChaMP, *open circle* and *triangle*), Hc (ChaMP+CDFs, *open square*), or He (Chiappetti et al. (2005), *open pentagon*) band. For the ChaMP, photon indices of  $\Gamma_{ph} = 1.4$  (*circles*) and  $\Gamma_{ph} = 1.7$  (*triangles*) were assumed. A photon index of  $\Gamma_{ph} = 1.7$  is assumed for Chiappetti et al. (2005) for self-consistency with their study. The solid line represents the line of equality for expected and measured break fluxes and is shown for illustrative comparison. The energy bands are listed in Table 1.

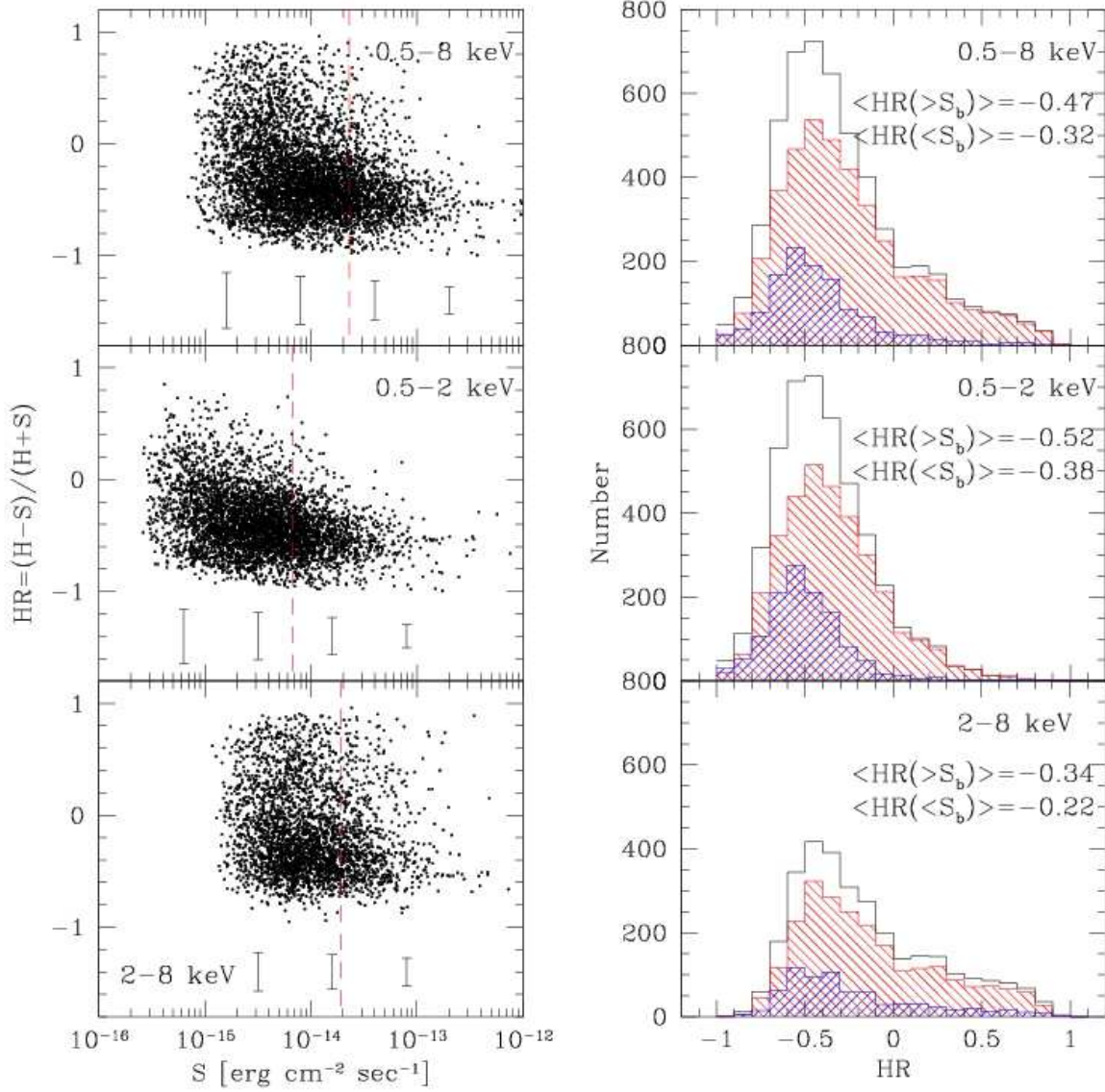


Fig. 11.— *left*. Hardness ratio (HR) distributions as a function of flux in three energy bands. A photon index of  $\Gamma_{ph} = 1.4$  was assumed. Error bars plotted at the bottom of each panel are the typical uncertainties of the hardness ratio at several flux bins. The vertical red dashed line indicates the break flux ( $S_b$  in Table 3) in each energy band. *right*. Hardness ratio distributions in the following flux ranges: entire flux range (*open histogram*),  $S < S_b$  (*red shaded histogram*), and  $S > S_b$  (*blue shaded histogram*). The median hardness ratio of the faint and bright samples are marked in each panel.

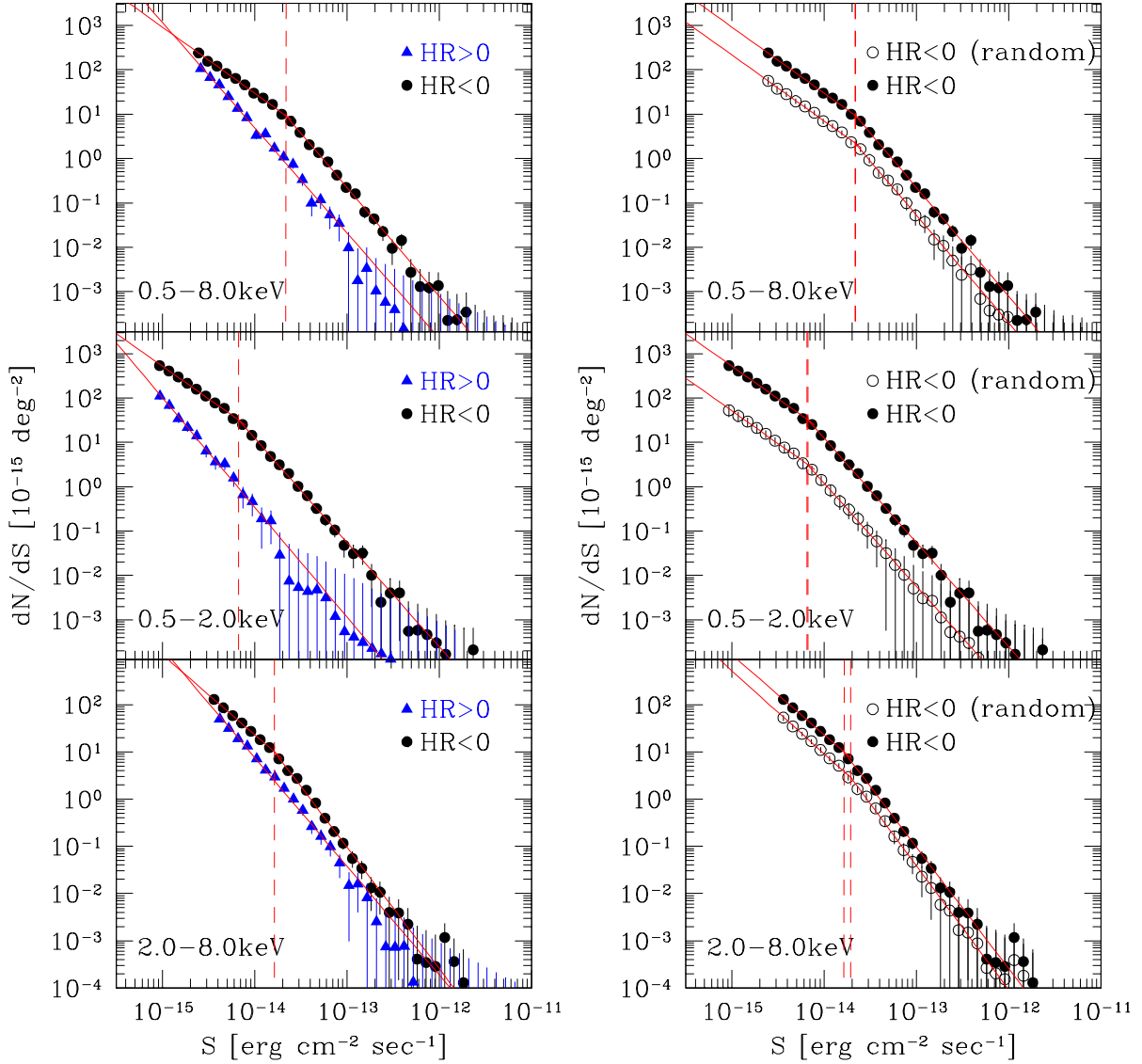


Fig. 12.— *left*. Differential number counts for the soft ( $HR < 0$ , *black circles*) and hard ( $HR > 0$ , *blue triangles*) sources in 3 energy bands. Soft sources show a break and are fitted with a broken power law while hard sources do not show a break and are fitted with a single power law. Red solid lines are the best fit results (see Table 5). The red vertical dashed line is the break flux in the soft source number counts. *right*. Averaged differential number counts from 1,000 random subsets of soft sources (*open circles*). Each subset has the same number of soft sources as hard sources. Even with the reduced statistics, soft sources still show a significant break and are fitted with a broken power law. The number counts for all soft sources (*filled circles*) is plotted in each energy band for comparison.

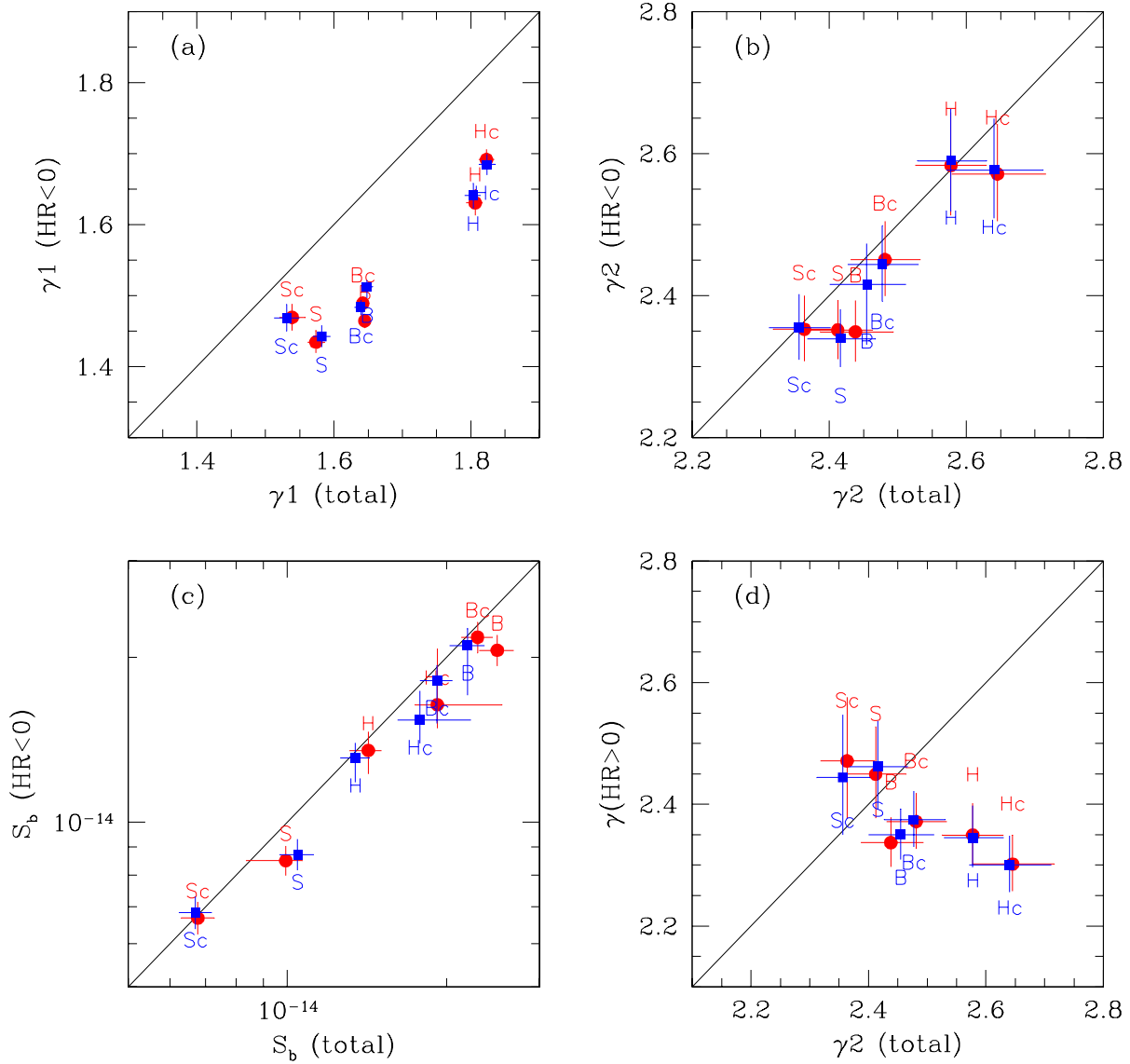


Fig. 13.— Comparison of the best fit parameters of the ChaMP differential number counts for the total sample (see Table 3) with those for subsamples (see Table 5). The total sample includes all sources regardless of the HR, the soft sample includes sources with  $HR < 0$ , and the hard sample includes sources with  $HR > 0$ . (a) Faint power law indices of the total sample vs. the soft sample. (b) Bright power law indices of the total sample vs. the soft sample. (c) Break flux of the total sample vs. the soft sample. (d) Bright power law indices of the total sample vs. single power law indices of the hard sample. The photon indices of  $\Gamma_{ph} = 1.4$  (red circles) and  $\Gamma_{ph} = 1.7$  (blue squares) are assumed. The solid line represents the line of equality for the two compared parameters and is shown for illustrative comparison.

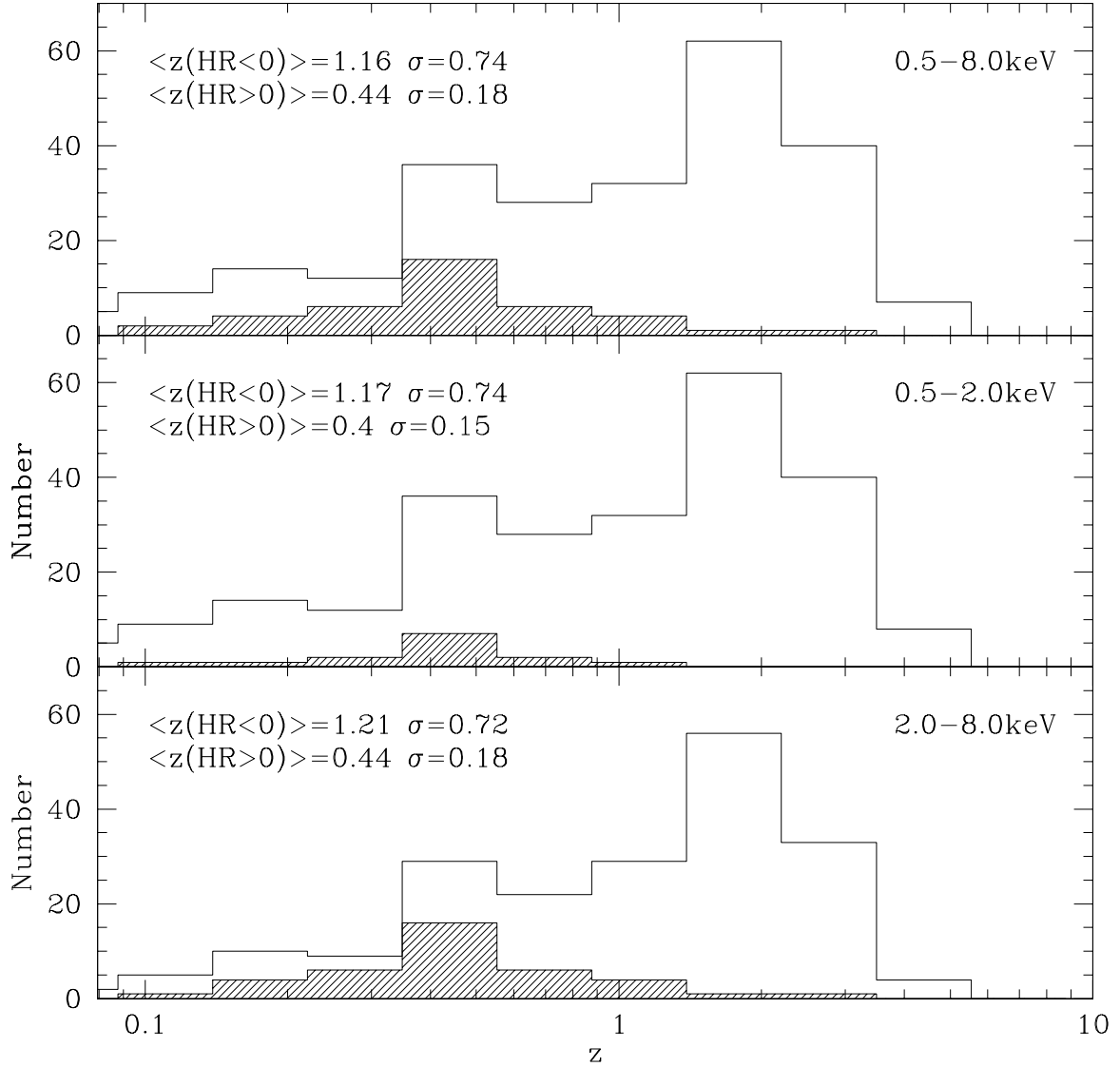


Fig. 14.— The redshift distributions of the soft ( $HR < 0$ , *open histogram*) and hard ( $HR > 0$ , *shaded histogram*) sources in the Bc (*top*), Sc (*middle*), and Hc (*bottom*) bands, respectively. The medians and standard deviations for each distribution are marked. Hard sources are distributed at lower redshifts compared to the soft sources in all energy bands. Sources with the highest optical counterpart match confidence levels and with the highest spectrum quality are only used.

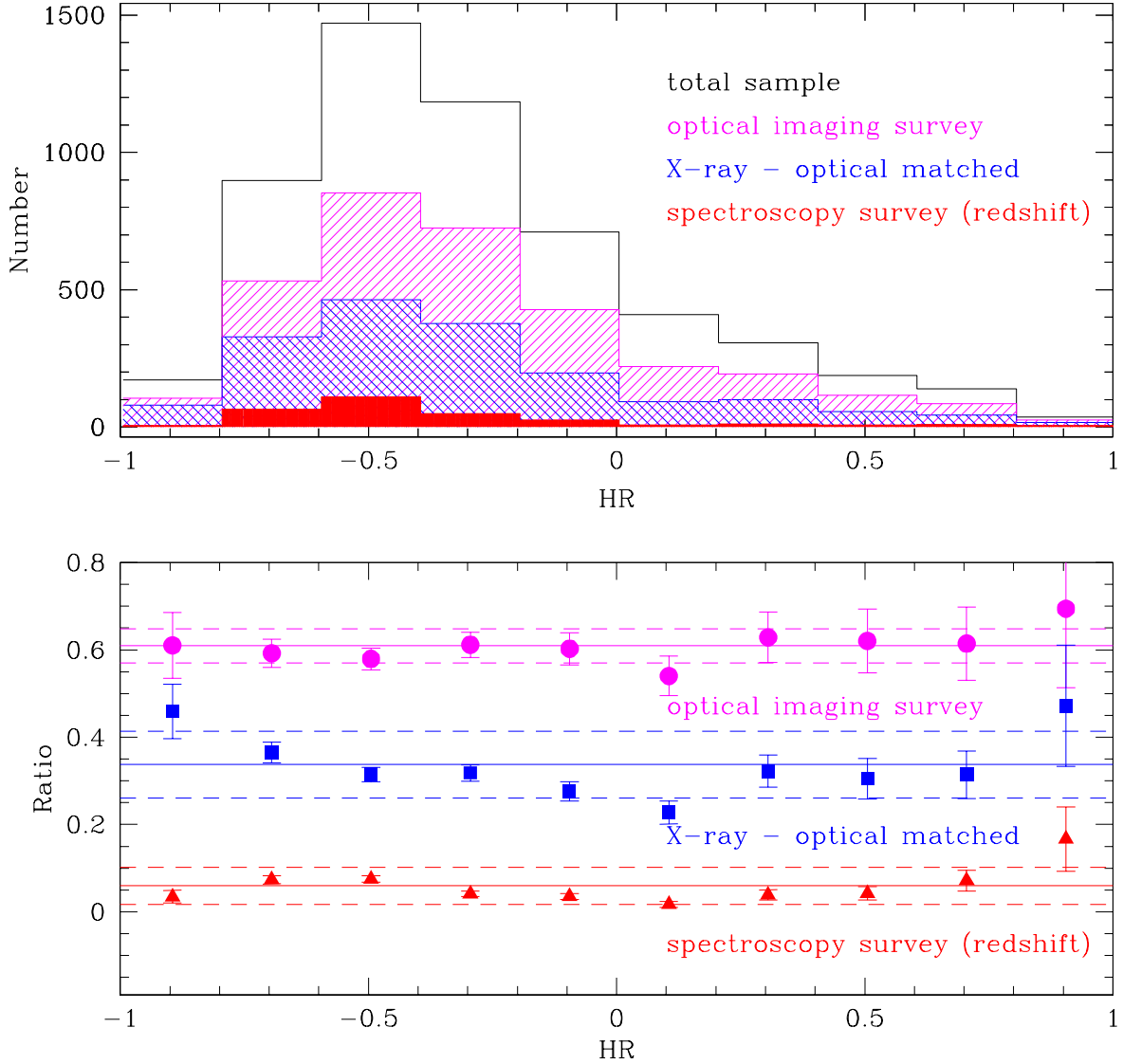


Fig. 15.— *top*. Hardness ratio distribution of the ChaMP sources in the B (0.3-8 keV) band in the following categories: total sample (*open histogram*), sources in 63 ChaMP fields with optical imaging observations (*magenta shade histogram*), sources having optical counterparts (*blue shade histogram*), and sources having redshifts (*red filled histogram*). *bottom*. The number ratios of the last three subsamples over total sample in each hardness ratio bin. The mean (*solid line*) and standard deviations (*dashed lines*) of each ratio are plotted. For the X-ray-optical matched sample and the redshift sample, only sources with the highest match confidence levels and with the highest spectrum quality are used.



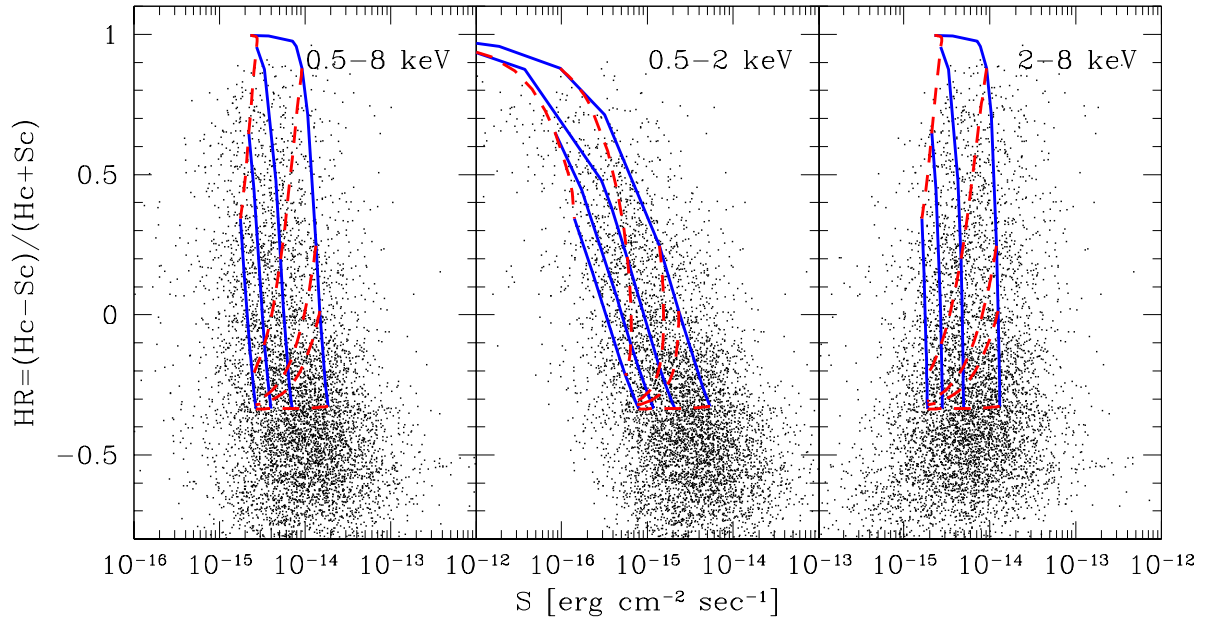


Fig. 16.— The flux-hardness ratio (S-HR) diagram for the ChaMP sources with  $S/N > 0$  (*black dots*) in the 0.5-8 keV (*left*), 0.5-2 keV (*middle*), and 2-8 keV (*right*), respectively. The grid indicates the predicted location of a test X-ray source for various redshift ( $z = 0, 1, 2$ , and  $3$ , blue solid lines from right to left) and intrinsic absorption ( $\log N_{H,int} = 20, 21.7, 22, 22.7$ , and  $23.7$ , red dashed lines from bottom to top). A photon index of  $\Gamma_{ph} = 1.4$  was assumed for the test source spectrum. The source becomes fainter with increasing intrinsic absorption and with increasing redshift. The source becomes harder with increasing intrinsic absorption; but, softer with increasing redshift. These effects are significant in the soft band. We note that the grid illustrates only a test source to indicate trends but does not cover the full range of the ChaMP sources.

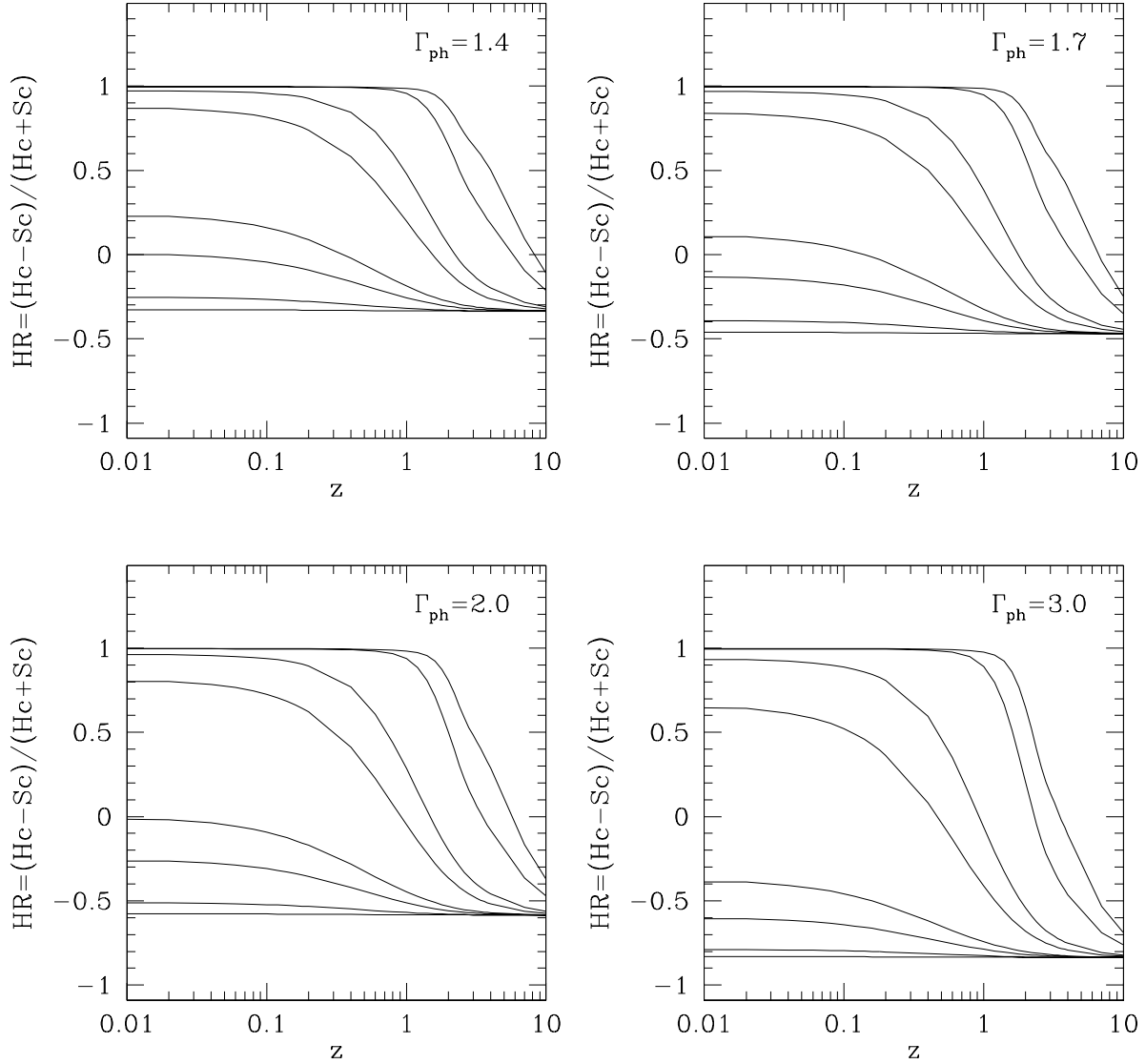


Fig. 17.— The hardness ratio of the test X-ray source as a function of redshift for photon indices of  $\Gamma_{ph} = 1.4$  (top left), 1.7 (top right), 2.0 (bottom left), and 3.0 (bottom right), respectively. In each panel, seven lines represent intrinsic absorptions of  $\log N_{H,int} = 20, 21, 21.7, 22, 22.7, 23, 23.7$ , and 24, respectively, from bottom to top. The test source becomes harder with increasing intrinsic absorption and with increasing redshift. The intrinsically hard source with high redshift is observed as a soft source in the observed frame due to the cosmological redshift.

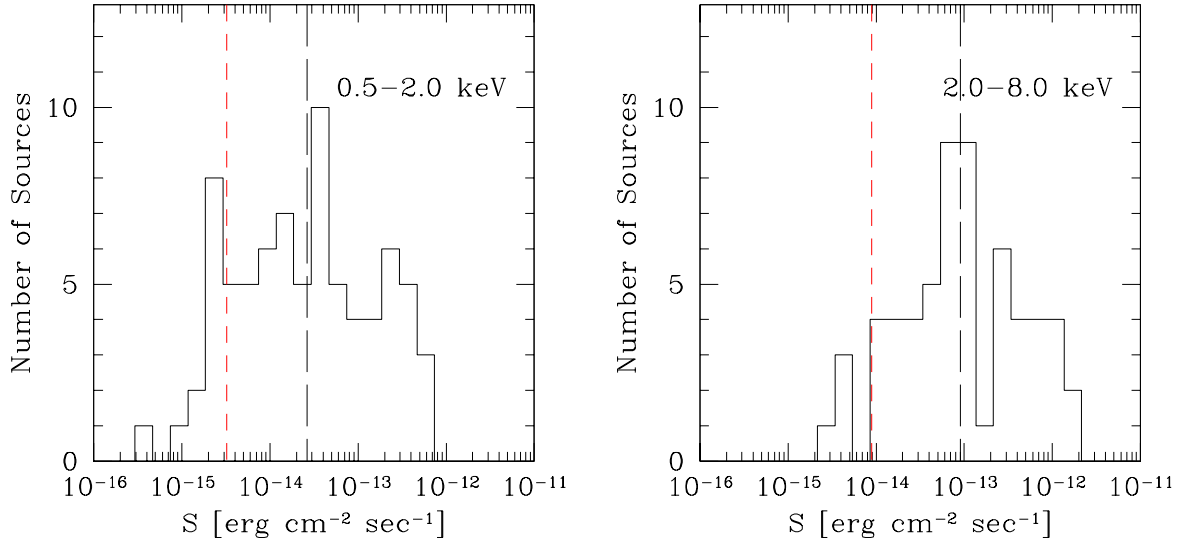


Fig. 18.— The flux distribution of target sources in the Sc (*left*) and the Hc (*right*) bands, respectively. The vertical lines indicate the median values of target (*black long dashed line*) and non-target (*red short dashed line*) sources (see the left panels of Figure 1 and Table 2 for non-target sources), respectively. Target sources have brighter fluxes compared with non-target sources.

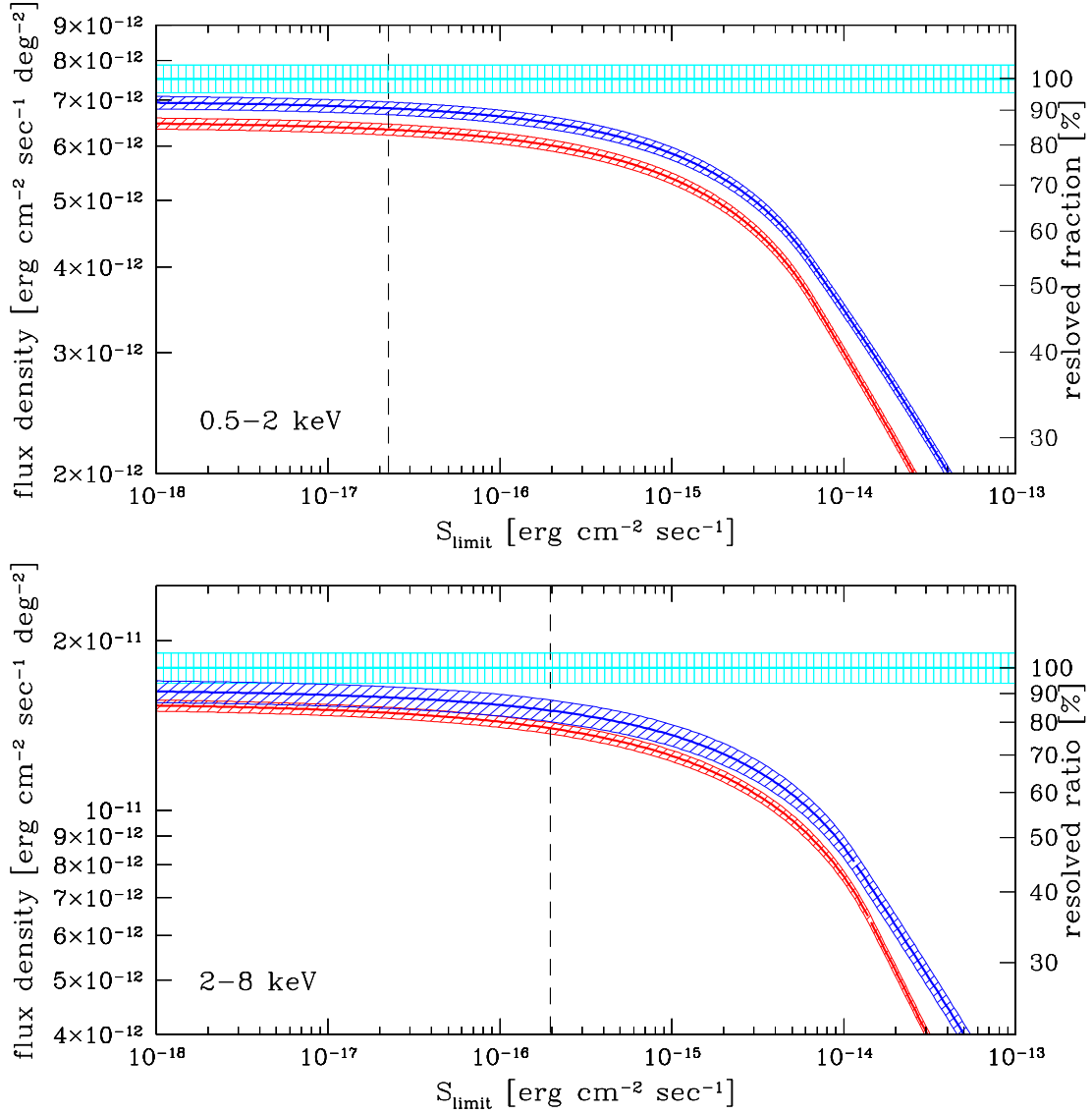


Fig. 19.— The resolved CXRB flux density from the ChaMP+CDFs number counts as a function of flux limit in the 0.5-2 keV (*top*) and 2-8 keV (*bottom*) bands. Blue and red shading represents the resolved CXRB with and without targets within  $\pm 1\sigma$  uncertainties, respectively. The cyan shaded level represents the total CXRB and the  $\pm 1\sigma$  confidence range from the literature (B04). The vertical dashed line indicates the faint flux limit of the ChaMP+CDFs. Below the faint flux limits, the results are extrapolated. A photon index of  $\Gamma_{ph} = 1.4$  was assumed.

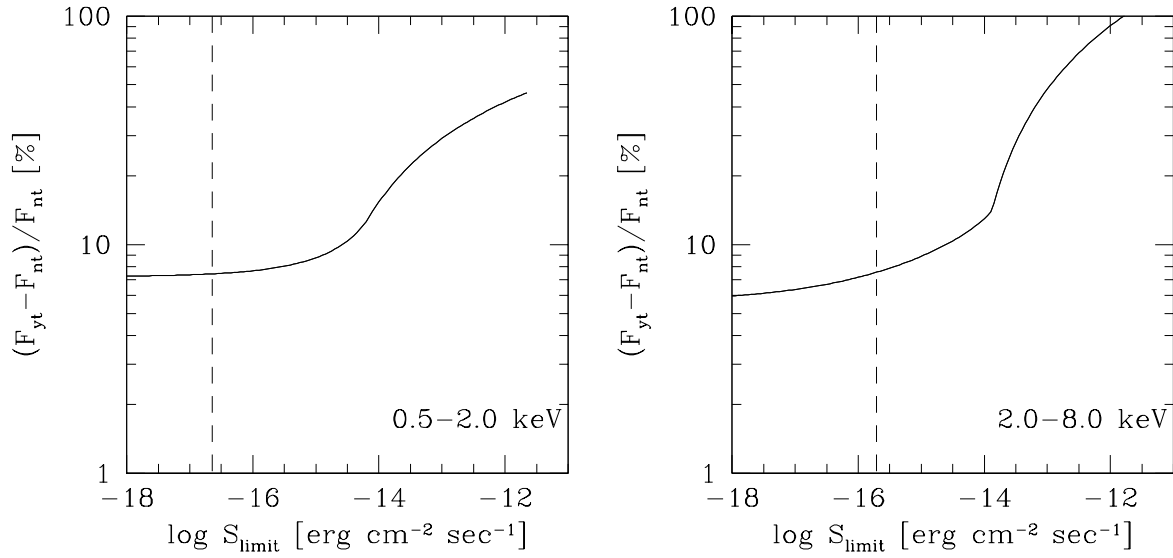


Fig. 20.— The fractional difference between the resolved CXRB excluding ( $F_{nt}$ ) and including ( $F_{yt}$ ) target sources, normalized to that of excluding targets in the 0.5–2 keV (*left*) and in the 2–8 keV (*right*) bands, respectively. The differences are extrapolated below the faint flux limits (vertical dashed lines). At the faint flux limits, the target source fractions are 7% (0.5–2 keV) and 6% (2–8 keV), respectively.

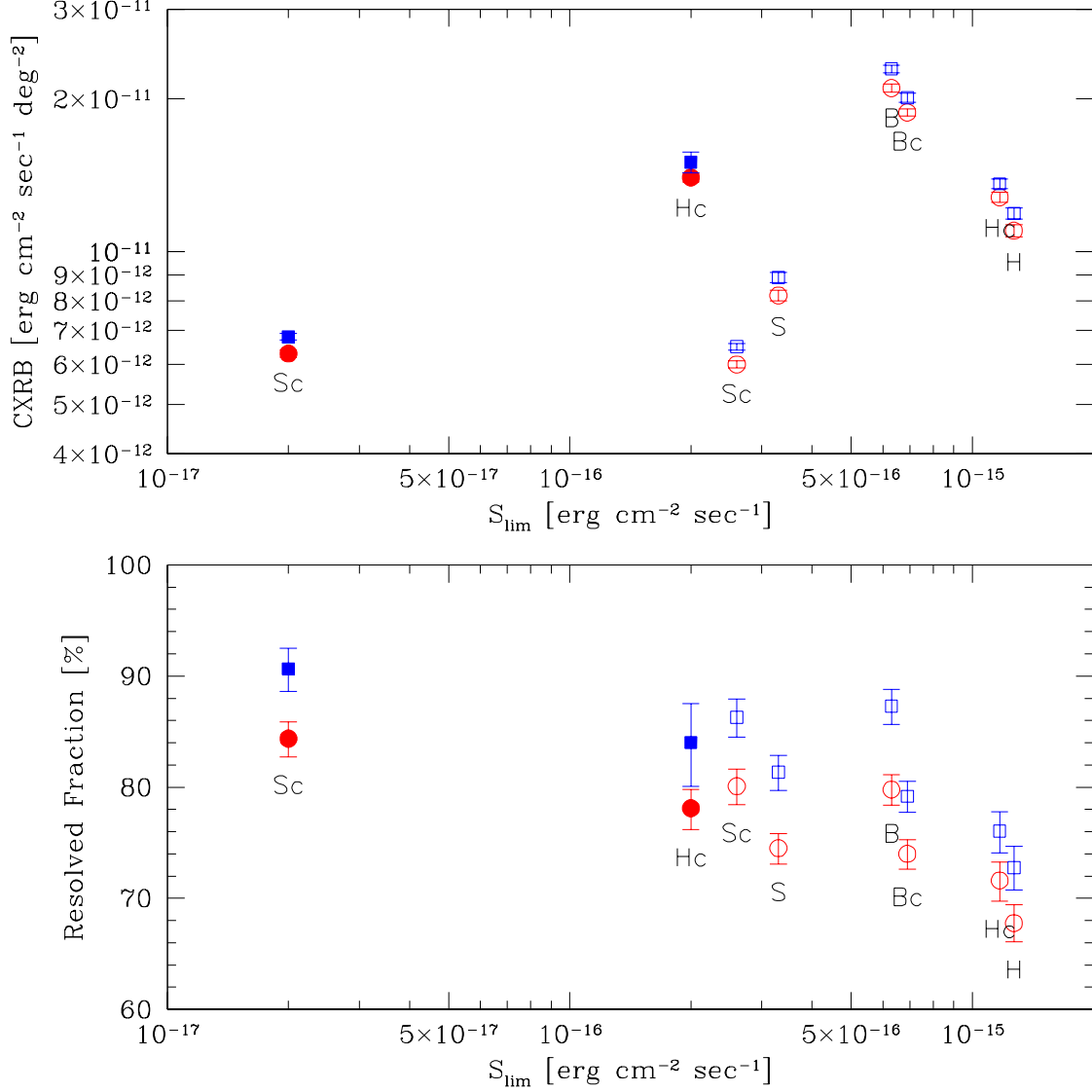


Fig. 21.— *top*. The resolved CXRB flux density from the ChaMP (*open symbols*) and the ChaMP+CDFs (*filled symbols*) number counts with target (*blue squares*) and without target (*red circles*) as a function of faint flux limit in 6 energy bands. *bottom*. The percentage of the total CXRB flux density that is provided by the resolved sources of the ChaMP and ChaMP+CDFs samples. The total CXRB in the Sc and Hc bands are from B04. In other bands, the total CXRB was derived by summing (Bc) or rescaling (B, S, and H) with those in the Sc and Hc bands (see §6.1). Symbols are the same as the top panel. For the definition of the energy band, see Table 1.

